

Deep weakly-supervised learning methods for classification and localization in histology images: a survey

Jérôme Rony^{a,*}, Soufiane Belharbi^a, Jose Dolz^a, Ismail Ben Ayed^a, Luke McCaffrey^b, Eric Granger^a

^a*Laboratoire d'imagerie, de vision et d'intelligence artificielle, École de technologie supérieure, Université du Québec, Montréal, Canada*

^b*Rosalind and Morris Goodman Cancer Research Centre, Dept. of Oncology, McGill University, Montréal, Canada*

Abstract

Using state-of-the-art deep learning models for the computer-assisted diagnosis of diseases like cancer raises several challenges related to the nature and availability of labeled histology images. In particular, cancer grading and localization in these images normally relies on both image- and pixel-level labels, the latter requiring a costly annotation process. In this survey, deep weakly-supervised learning (WSL) architectures are investigated to identify and locate diseases in histology image, without the need for pixel-level annotations. Given a training dataset with globally-annotated images, these models allow to simultaneously classify histology images, while localizing the corresponding regions of interest. These models are organized into two main approaches that differ in their mechanism for building attention maps to localize salient regions of interest – (1) bottom-up approaches (based on forward-pass information through a network, either by spatial pooling of representations/scores, or by detecting class regions), and (2) top-down approaches (based on backward-pass information within a network, inspired by human visual attention). Since relevant WSL models have mainly been developed in the computer vision community, and validated on natural scene images, we assess the extent to which they apply to histology images which have challenging properties, e.g., large size, non-salient and highly unstructured regions, stain heterogeneity, and coarse/ambiguous labels. The most relevant deep WSL models (e.g., CAM, WILDCAT and Deep MIL) are compared experimentally in terms of accuracy (classification and pixel-level localization) on several public benchmark histology datasets for breast and colon cancer (BACH ICIAR 2018, BreakHis, CAMELYON16, and GlaS). Results indicate that several deep learning models, and in particular WILDCAT and deep MIL can provide a high level of classification accuracy, although pixel-wise localization of cancer regions remains an issue for such images.

Keywords: Medical/Histology Image Analysis, Computer Aided Diagnosis, Machine Learning, Multiple Instance Learning, Deep Learning, Image Classification, Weakly Supervised Pixel-level Localization

1. Introduction

The advent of Whole Slide Imaging (WSI) scanners (He et al., 2012), which can perform cost-effective and high-throughput digitization of histology slides, has opened new possibilities in pathology image analysis (He et al., 2012; Madabhushi, 2009). Histology slides provide more comprehensive view of diseases and their effect on tissue (Hipp et al., 2011), since their preparation preserves the underlying tissue structure (He et al., 2012). For instance, some

disease characteristics, e.g., lymphatic infiltration of cancer, may be predicted using only histology images (Gurcan et al., 2009). The diagnosis from a histology image remains the gold standard in diagnosing several diseases including most types of cancer (He et al., 2012; Gurcan et al., 2009; Veta et al., 2014). Breast cancer is the most prevalent cancer in women in worldwide. Medical imaging systems are a primary diagnosis tool for its early detection (Daisuke and Shumpei, 2018; Veta et al., 2014; Xie et al., 2019).

Fig.1 shows examples of three different types of medical imaging: computed tomography (CT), cytology, and histology images. The three imaging

*Corresponding author:
Email address: jerome.rony.1@etsmtl.net (Jérôme Rony)

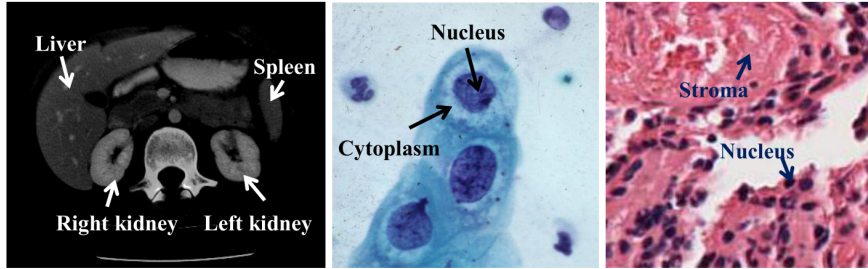


Figure 1: Image examples for radiology CT (left), cytology (middle), and histology (right). (Credit: (He et al., 2012, 2010))

operate in different resolutions: CT, and magnetic resonance image (MRI) at whole body, and tissue level; histology at tissue-cell level; cytology at cellular level. Histology images differ from radiology images in having a large amount of objects of interest (cells and cell structures, such as nuclei) widely distributed and surrounded by various tissue types (for example, in the cervix, epithelium and stroma). In contrast, radiology image analysis usually focuses on a few organs in the image, which tend to be more predictably located compared to histology images, where objects constantly change location. A histology image usually has a size of $\sim 10^9$ pixels which is significantly larger than that of a radiology image $\sim 10^5$ pixels. In addition, histology tissues are generally stained with different, but in the same palette, colors while radiology images usually contain only gray intensities. On the other hand, cytology images have some similarities to histology images; both have multiple cells distributed within the image. However, histology images are often taken at much lower level of magnification level to allow analysis at the tissue level, and identification of the boundary between tissue types. The level of magnification is sufficient for some analysis at the cell level, such as nucleus counting, but can not provide the in-depth information of internal cell structure.

Cancer is mainly diagnosed by pathologists who must analyze WSIs, often identifying groups of cells organized in ducts or lobules within a heterogeneous stroma. Analysing WSIs from a digitized histology slides allows to facilitate, and potentially automate, computer-aided diagnosis (CAD) in pathology, where the main goal is to confirm the presence or absence of disease, and to grade or measure disease progression. The widespread use of CAD can be traced back to the emergence of digital mammography in the 1990s (Méndez et al., 1998). Since a large number of digitized exams have been collected, CAD has become a part of the routine clinical detection of

breast cancer, for instance at many screening sites and hospitals (Tang et al., 2009). Fig.2 presents the standard processing chain of a CAD system.

While the interpretation of histology images remains the standard for cancer diagnosis, current computer technology towards this task falls behind clinical needs. Manual analysis of histology tissues depends heavily on the expertise and experience of histopathologists. Such manual interpretation is time consuming and difficult to grade in a reproducible manner. Empirically, it is known that there are substantial intra- and inter-observation variations among experts. Such factors impede the development of effective computer-based histology analysis along other factors: 1. the large diversity and high complexity of histology traits make it difficult to develop a universal computer system to analyze images of different cancers; 2. the fact that advanced image processing systems for radiology and cytology applications can not be directly adopted for histology images due to the different imaging technologies and image characteristics; 3. the scarcity of annotation of cancerous tissue identification and classification, which makes algorithm evaluation largely subjective or only dependable to minimal confidence testing; Nonetheless, the growing demands on experts to inspect the images had driven interest in CAD systems (Fig.2).

Automation of CAD systems can be traced back to the analysis of the spatial structure of histology images (Bartels et al., 1992; Hamilton et al., 1994; Weind et al., 1998). Techniques in image processing and machine learning (ML) have been leveraged to identify discriminative structures and classify histology images (He et al., 2012). These techniques range from thresholding (Gurcan et al., 2006; Petushi et al., 2006), to active contours (Bamford and Lovell, 2001), Bayesian classifiers (Naik et al., 2007), graphs to model the spatial structure (Bilgin et al., 2007; Tabesh et al., 2007), and ensemble methods

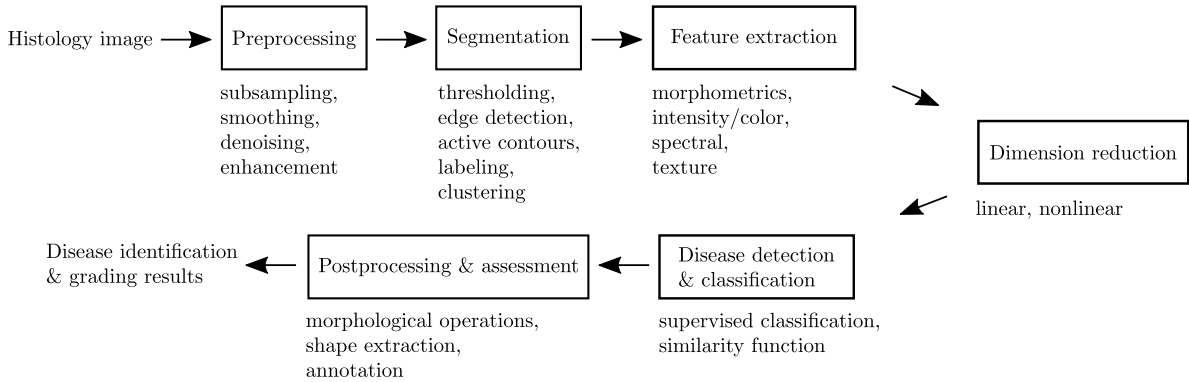


Figure 2: Typical processing steps for computer-aided diagnosis (He et al., 2012).

based on SVMs and Adaboost (Doyle et al., 2006b; Qureshi et al., 2008). An overview of techniques and their applications is provided in (He et al., 2012; Gurcan et al., 2009; Veta et al., 2014).

Deep learning (DL) models (Goodfellow et al., 2016), and in particular convolutional neural networks (CNNs), provide state-of-the-art performance in many visual recognition applications, such as image classification (Krizhevsky et al., 2012), object detection (Redmon et al., 2016), and segmentation (Dolz et al., 2018). These supervised learning architectures are trained end-to-end with large amounts of annotated (labeled) training data to encode a hierarchy of discriminant image features representing different levels of abstraction. More recently, the potential of DL models has begun to be explored in assisted pathology diagnosis (Janowczyk and Madabhushi, 2016; Daisuke and Shumpei, 2018; Li and Ping, 2018). Given the growing availability of histology slides, DL models for CAD have not only been proposed for disease prediction (Hou et al., 2016; Li and Ping, 2018; Sheikhzadeh et al., 2016; Spanhol et al., 2016a; Xu et al., 2016), but also for related tasks like detection and segmentation of tumor regions within WSI (Kieffer et al., 2017; Mungle et al., 2017), scoring of immunostaining (Sheikhzadeh et al., 2016; Wang et al., 2015), cancer staging (Shah et al., 2017; Spanhol et al., 2016a), mitosis detection (Chen et al., 2016; Cireşan et al., 2013; Roux et al., 2013), gland segmentation (Caie et al., 2014; Gertych et al., 2015; Sirinukunwattana et al., 2017), and detection and quantification of vascular invasion (Caicedo et al., 2011).

Histology images differ from natural scene images because the regions of interest (tumors) are not structured or salient. ML techniques proposed to analyze histology images often require full super-

vision to address key tasks, such as classification, localization¹ and segmentation (Janowczyk and Madabhushi, 2016; Daisuke and Shumpei, 2018). Learning to accurately localize cancer regions of interest normally requires dense pixel-level annotation of images. In order to train a CNN to, e.g., localize or segment cancerous regions, one typically requires a large amount of histology images with pixel-level labels to optimize the parameters of a DL model. It is however clear that training powerful DL models to predict the image class, and locate image regions linked to these predictions, *without* dense annotation is highly beneficial in histology image analysis. These image-level labels can easily be obtained by pathologists during analysis. Therefore, training datasets in this domain are often comprised of large images that are coarsely-annotated according to the diagnosis. Considering the size and complexity of such images, dense annotation of images comes at a considerable cost, and requires a highly trained expert. Outsourcing this task to standard workers such as Mechanical Turk Worker is not an option.

In this paper, we focus on DL models that can be trained using data with image-level labels in order to classify a histology image while localizing the corresponding regions of interest within the image. Techniques for weakly-supervised learning (WSL) are very promising for this purpose because they exploit unlabeled inputs, and coarse and ambiguous labels. They are applied in scenarios involving either (1) incomplete supervision (when only a small subset of training data has labels, although unlabeled

¹Object localization typically consists in isolating an object of interest by providing the coordinates of its surrounding bounding box. In this survey, it is also understood as a task providing pixel-level segmentation of the object, which provides a more accurate region localization.

data is abundant), (2) inexact supervision (when training with labeled data with coarse labels), and (3) ambiguous or inaccurate supervision (when labels may suffer from errors or noise) (Zhou, 2017). The inexact supervision scenario is relevant in this paper, where training datasets only require global image-level annotations. Under this scenario, powerful techniques for multiple-instance learning (MIL) (Carboneau et al., 2018; Cheplygina et al., 2019; Wang et al., 2018; Zhou, 2004) are generally considered, where individual instance labels (e.g., image pixels, segments or patches) are not observable or do not belong to well defined classes – training instances are grouped into sets (e.g., images), and supervision is only provided for sets of instances.

While there has been different reviews for the application of machine learning and deep learning in medical domain in particular in histology slides analysis (Janowczyk and Madabhushi, 2016; Kandemir and Hamprecht, 2015; Daisuke and Shumpei, 2018; Sudharshan et al., 2019; Litjens et al., 2017) and medical video (Quellec et al., 2017), they are often limited to fully supervised learning scenarios such as classification or segmentation; semi-supervised learning scenario (Litjens et al., 2017) in diagnosis and segmentation in medical domain. Up to our knowledge, we believe that we are the first to make a survey specifically for weakly supervised localization of regions of interest in histology images using deep learning using deep learning techniques. Most the techniques in these reviews and this survey rely heavily and overall on MIL framework either explicitly by using its formulation or implicitly by splitting the entire image into instances for learning.

Deep weakly-supervised learning (WSL) techniques (Cheplygina et al., 2019; Zhou, 2017) also provide the advantage of *interpretability* (Zhang and Zhu, 2018). Despite the success of deep NNs in many different applications, they are often seen as a black boxes that lack the ability to provide explanatory factors of their decisions (Lipton, 2018; Marcus, 2018, 2001; Ribeiro et al., 2016; Samek et al., 2017). The transparency issue (i.e., the absence of clear explanatory factors of a model’s decision) is a potential liability for ML models in critical in medical image analysis application (O’Neil, 2016). *Interpretable ML* (Doshi-Velez and Kim, 2017; Molnar et al., 2018) is an emerging branch of ML that aims to promote the design of interpretable ML models, and provide new techniques to explain model’s decisions. In computer vision, visual attention maps represent one of such methods developed to *localize*

reliable regions within the image used by the network to make its prediction (Zhang and Zhu, 2018). The deep WSL models investigated in this paper produce an attention map where high magnitude responses correspond to image regions of interest. One can thereby extract region locations and segments without the need to pixel-level annotation (Zhou et al., 2016). From medical perspective, region localization can provide a direct support (i.e., an explanatory factor) to the model’s prediction of the cancer type, a highly desired property in a CAD system. For instance, regions of interest can later be discarded by the pathologist if they are benign, or be inspected if they indicate cancerous regions.

This paper provides a survey of state-of-the-art deep WSL models that are suitable for the identification of diseases (e.g., type of cancer) in whole slide histology images, and localization of regions of interest that support the predicted disease. Given a dataset of globally-annotated training images, these models allow to simultaneously classifying images while localizing the corresponding regions of interest. Two types of WSL approaches have been proposed in literature that build attention maps to localize regions – (1) bottom-up approaches – like WILDCAT (Durand et al., 2017) and deep MIL (Ilse et al., 2018) – that use forward-pass information, either by spatial pooling of representations/scores², or by detecting class regions), and (2) top-down approaches – like Grad-CAM (Chattopadhyay et al., 2018; Selvaraju et al., 2017) – that use backward information, and are inspired by human visual attention. The most relevant models are compared experimentally in terms of accuracy for image classification, pixel-level localization of regions, and complexity on several public benchmark histology datasets for breast and colon cancer. Unfortunately, histology datasets with both image- and pixel-level labels are rare, and several benchmarks are private. In order to provide more histology image benchmarks for large scale evaluations of WSL methods, we also propose a protocol to build WSL datasets from WSIs. Our deterministic code and the coordinates of sampled patches from CAMELYON16 dataset are publicly available. Models from literature have mainly been developed in computer vision community, and validated on natural scene images. Consequently, experiments allow investigating the extent to which these

²Such category of methods do not rely on any priors on the nature of the images at hand, which make them a plug-and-play methods.

methods can be applied to histology images which have different properties and challenges: large size, non-salient and highly unstructured regions, stain heterogeneity, and coarse/ambiguous labels.

This survey is organized as follows. Sec.2 provides some background of histology image production and analysis, as well as key challenges. In Sec.3, different models for deep Weakly supervised localization are described and analyzed with histology image analysis in mind. Finally, Sec.4 presents the experimental methodology for our comparative study (datasets, protocols and performance metrics), while Sec.5 presents quantitative and qualitative results, interpretation, and future research directions.

2. Histology image analysis – background and challenges

Cytology imagery provides interesting characteristics that ease the visual analysis, like isolated/clustered cells and the absence of complicated structures such as glands. Moreover, this type of image often results from the least invasive biopsies, contributing to their common use in disease screening and biopsy purposes (Gurcan et al., 2009). Compared to cytology imagery, histology slides provide a more comprehensive view of diseases and their effect on tissue (Hipp et al., 2011), since their preparation preserves the underlying tissue structure (He et al., 2012). Histological analysis is performed by inspecting a thin slice (i.e., section) of tissue under an optical or electron microscope (Kiernan, 1990; Murphy and Davidson, 2001; Mescher, 2013; Gartner and Hiatt, 2006; Sternberg, 1997). The study of histology images is considered as the gold standard for clinical diagnosis of cancer and identification of prognostic and therapeutic targets. Histopathology, the microscopic study of biopsies to locate and classify diseases, has roots in both clinical medicine and basic science (Sternberg, 1997). In this section, we first summarize the production of histology images, from tissue preparation to imaging technologies. Then, we briefly review histology image analysis, its relation to other types of medical imaging, and its main challenges.

2.1. Image production:

Fig.3 presents an overview of the process of obtaining histology images. Fixation is the first stage of preparation for subsequent procedures, which should be conducted in real time to preserve the samples as

well as possible. Different fixatives (e.g., precipitant and crosslinking) or methods (e.g. heat fixation and immersion) may be used. For example, the precipitant fixatives (e.g., methanol, ethanol, acetone, and chloroform) dehydrate the tissue samples, removing lipid and reducing the solubility of proteins. After fixation, the tissue must be adequately supported, e.g., frozen or embedded in a solid mold, to allow sufficiently thin sections to be cut for microscopic examination. Common treatments employ a series of reagents to process the fixed tissue and embed it in a stable medium such as paraffin wax, plastic, or resin. Such treatments include the main steps of dehydration³, clearing, infiltration, and embedding (Chandler and Roberson, 2009; Nelson et al., 2008; Woottton et al., 1995).

The embedded tissue sample is finally cut into thin sections (e.g., $5\mu\text{m}$ for light microscopy and $80 - 100\text{nm}$ for electron microscopy). The transparent sections are usually produced with a microtome, an apparatus feeding the hardened blocks through a blade with high precision. After cutting, the sections are floated in warm water to smooth out any wrinkles. Then, they are mounted (by heating or adhesives) on a glass slide. Once they are attached on the slide, the process is reversed prior to staining. The wax is removed with a solvent (usually xylenes) and the tissue is re-hydrated through a series of solutions in which the alcohol:water ratio is changed. The gradual rehydration preserves tissue architecture. Now, the sections are ready for staining, which helps to enhance the contrast and highlight specific intra- or extra-cellular structures. A variety of dyes and associated staining protocols are used. The routine stain for light microscopy is hematoxylin and eosin (H&E); other stains are referred to as special stains for specific diagnostic needs. Each dye binds to particular cellular structures, and the color response to a given stain can vary across tissue structures. For example, hematoxylin stains the nuclear components of cells dark blue and eosin stains the cytoplasmic organelles varying shades of pink, red, or orange. (Kiernan, 1990; Ross et al., 2003) provide a detailed description of common laboratory stains. After staining, the stained section on the slide is covered to protect the tissue and provide better visual quality for microscope examination.

After the tissue has been prepared, light microscope (Murphy and Davidson, 2001; Török and Kao,

³The purpose of dehydration is to remove water so that the parafin wax can infiltrate.

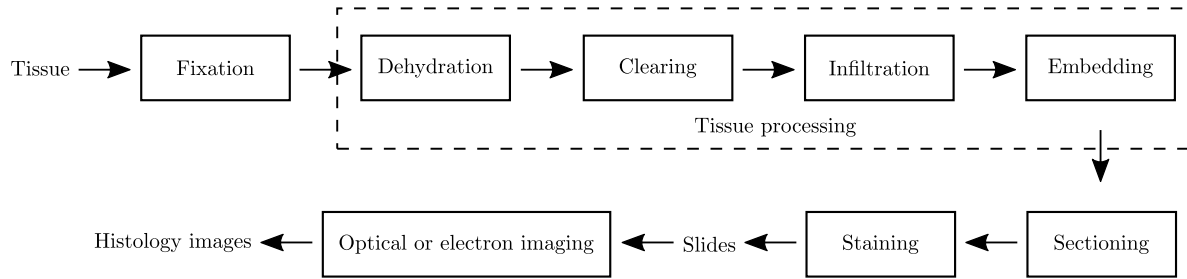


Figure 3: Histology tissue preparation and image production (He et al., 2012, 2010).

2007), is used to take digital histology images of the stained sections. Additional details on different types of microscopes and image production are provided in (He et al., 2012, 2010).

2.2. Image analysis:

In histology image analysis for cancer diagnosis, histopathologists visually inspect the regularities of cell shapes and tissue distributions. Such histopathological study has been extensively employed for cancer detection and grading applications, including prostate (Doyle et al., 2007, 2006a), breast (Basantanahally et al., 2008; Doyle et al., 2008), cervix (Guillaud et al., 2005, 2004), and lung (Jütting et al., 1999; Kayser et al., 2002) cancer grading, neuroblastoma categorization (Gurcan et al., 2006; Kong et al., 2007b), and follicular lymphoma grading (Cooper et al., 2009; Kong et al., 2007a).

Histopathology problems have been an attractive research field from different disciplines including clinical medicine, biology, chemistry, and machine learning. Computer-based image analysis has become an increasingly important field due to the high rate of production and the increasing reliance on these images by the biomedical community. Medical image processing and analysis in radiology (e.g., X-ray, ultrasound, CT, MRI), and cytology have been active research fields for several decades and numerous systems (Bankman, 2008; Greenberg, 1984; He, 2009; Yoo, 2004) and products⁴⁵⁶ (Lamprecht et al., 2007; Schroeder et al., 2003) have been developed. However, the application of these systems in histology analysis is not straightforward due to the significant difference in the imaging techniques and image characteristics.

The complexity of histology images is defined by several factors, including overlapping tissue types and cell boundaries and nuclei corrupted by noise; some structures, such as cell boundaries, may appear connected or blurred. These factors make it rather difficult to extract cell regions (e.g., nuclei and cytoplasm) by traditional image segmentation approaches. On the other hand, cytology images are taken at high magnification level which results in clearly identified cell compartments. Computer-based histology analysis systems generally exploit a much larger quantity of image features to derive clinically meaningful information than similar systems for radiology and cytology (He et al., 2012). Nevertheless, the image analysis systems for these three domains generally consist of a common sequence of steps of image restoration, segmentation, feature extraction, and pattern classification (see Fig.2).

2.3. Key challenges:

Histology image analysis has attracted much recent attention in the ML and computer vision communities (Daisuke and Shumpei, 2018; Litjens et al., 2017; Spanhol et al., 2016a; Sudharshan et al., 2019), resulting in open competitions and public datasets such as GlaS (Sririkunwattana et al., 2017), TUPAC16 (Veta et al., 2018), CAMELYON (Bándi et al., 2019; Ehteshami Bejnordi et al., 2017), and BACH 2018 (Aresta et al., 2018). The following describes the main difficulties of designing ML models for visual recognition using such image data.

High resolution images. Pathology images come often in high resolution (WSI, Fig.4), leading to difficulties in term of memory storage and processing time. A WSI has a higher resolution than the most common medical imaging type. For instance, the largest radiological image datasets obtained on a routine basis are high resolution chest CT scans

⁴ImageJ (<https://rsbweb.nih.gov/ij/>).

⁵Medical Image Processing, Analysis and Visualization (<https://mipav.cit.nih.gov>) (MIPAV).

⁶ CellProfiler: Cell Image Analysis Software (<https://www.cellprofiler.org>).

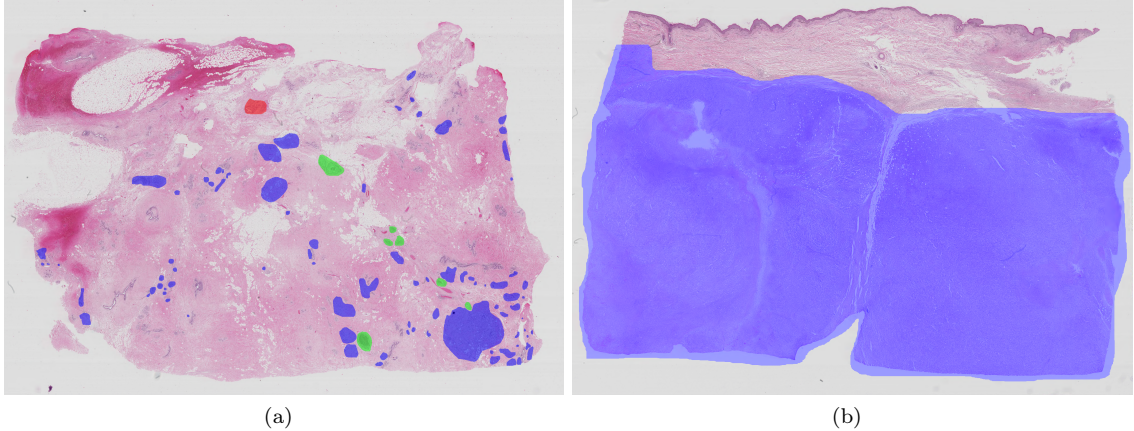


Figure 4: Segmentation of two WSI from the ICIAR 2018 BACH Challenge. Colors represent cancerous regions of different types: red for **Benign**, green for **In Situ Carcinoma** and blue for **Invasive Carcinoma**. We can see an important difference in the size and presence of regions (Aresta et al., 2018).

comprising approximately $(512, 512, 512)$ spatial elements (~ 134 million voxels). In contrast, a single core of prostate biopsy tissue digitized at $40\times$ resolution is approximately $(15,000, 15,000)$ elements (~ 225 million pixels). To put this in context, a single prostate biopsy procedure can comprise anywhere between 12 and 20 biopsy samples or approximately 2.5–4 billion pixels of data generated per patient study (Hipp et al., 2011; Gurcan et al., 2009). In practice, this issue is addressed either by down-sampling to lower resolution WSI, which results on a significant loss of image details, or by preserving such details and losing the spatial information of the entire WSI by sampling patches from the WSI. A potential issue in sampling patches is that the WSI labels are not transferred correctly to the patch. A sampled patch from a WSI with cancerous label may contain only healthy tissue, however, it will be assigned the class of the WSI. This inconsistency in patch labeling can mislead ML models during the training process, and decrease the model’s performance (Freney and Verleysen, 2014; Sukhbaatar et al., 2014; Zhang et al., 2017). Moreover, the high resolution of WSI makes pixel-level annotation impractical and extremely time consuming. In practice, the WSI annotation is coarse and scarce (i.e., the overall diagnosis) (Fig.4). This prevents from obtaining large corpora for training accurate ML models for segmentation and localization of image regions.

Heterogeneous data. Another key challenge in histology image analysis is related to the heterogeneity of data due to variations in staining. As

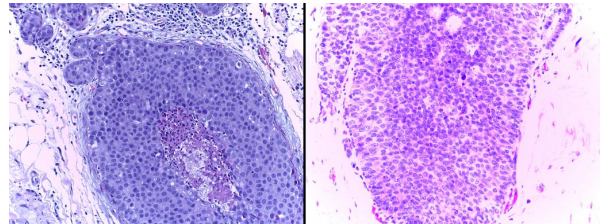


Figure 5: Difference in staining for two images labeled both as *In Situ Carcinoma* extracted from different WSI (Aresta et al., 2018).

described in Sec.2.1, histology images are produced after many processing steps. Since they involve different chemical processes, many variables may affect the resulting histology image stain including the target diagnosis, the operator, the laboratory, the type of used chemicals, the duration of exposure to them, the microscope, and many other factors. Fig.5 shows an example of such stain variation. While it is easy for pathologists to discard these variations, ML models can be heavily and negatively affected since they are sensitive to changes in the statistics of input signals (Shimodaira, 2000; Sugiyama and Kawanabe, 2012), in particular neural based models (Szegedy et al., 2013). In practice, this issue can be alleviated either by performing color normalization (Ciompi et al., 2017; Janowczyk et al., 2017) or color augmentation during training to improve robustness to stain variations. Among these strategies, color augmentation is particularly relevant when training using small datasets, through, e.g., randomly

Taxonomy

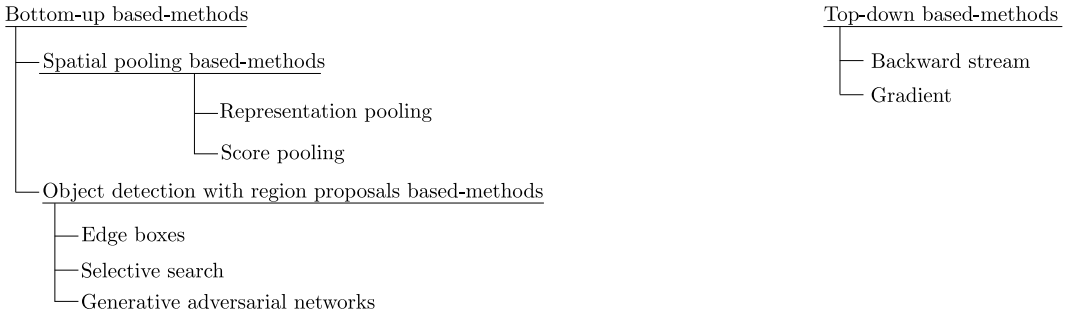


Figure 6: Overall taxonomy of deep weakly supervised localization models that rely on global image annotations.

modifying brightness, contrast, saturation and hue within chosen ranges.

Noisy annotations. Noisy or ambiguous annotations are a common practical issues in ML. In histology image analysis, such issue arises as a result of the way the pathologists grade WSIs. Often, such annotation is conducted by assigning the worst stage of cancer to the image. Therefore, a WSI that is labeled with a specific grade is more likely to contain most of the grades that are lower than the labeled grade. During training ML algorithms, often, sampling patches is a common strategy used to deal with large images. In such case, the WSI label is transferred to each patch. Such label transfer is not reliable, and it introduces noise and inconsistency into the patch label. Label inconsistency can degrade model performance and entangle learning (Frenay and Verleysen, 2014; Sukhbaatar et al., 2014; Zhang et al., 2017). Most of the time, a cancerous patch contains a relatively small cancerous region, while the rest is normal. The issue is aggravated when having many classes to characterize non-cancerous and cancerous lesions, e.g., **benign**, **in situ**, **invasive**, along with the normal class.

3. A survey of deep weakly supervised learning techniques for classification and localization

This section presents a review of state-of-the-art deep WSL models that can be trained to *simultaneously* perform two tasks – image classification and object localization – using only WSIs annotated with global labels. Most of these techniques have been proposed in literature to process natural images, and validated on well-known public benchmarks such as

ImageNet (Deng et al., 2009), Pascal VOC (Everingham et al., 2010), and MS-COCO (Lin et al., 2014). Since histology images have different characteristics than natural scene images, we first present the main categories of models for deep WSL in natural scene images, and then describe the models that are most relevant for our application. We end this section with a critical analysis and a selection of relevant models for experimental evaluation on histology datasets (Sec.3.4).

3.1. Overall taxonomy:

Among deep weakly supervised localization methods, we identify two main categories based on the way object localization is achieved (Fig. 7): bottom-up methods that are based on the forward pass information within a network, and top-down methods that are based on the backward information. Fig. 6 illustrates the overall taxonomy. All the different methods share two main common aspects. 1. **The localization mechanism:** in order to spot the object of interest, each method relies either on: (1) an attention map where high magnitude responses correspond to salient regions within the image –i.e., regions of interest– or (2) a bounding box that encloses the object of interest. 2. **The required training label:** each method can be trained using data with image-level annotation in order to classify an image while localizing the corresponding regions of interest within the image.

3.1.1. Bottom-up weakly supervised localization techniques:

With these methods, the pixel-wise localization is based on the activation of the feature maps due to the standard flow of information within a network from the input signal into the output target

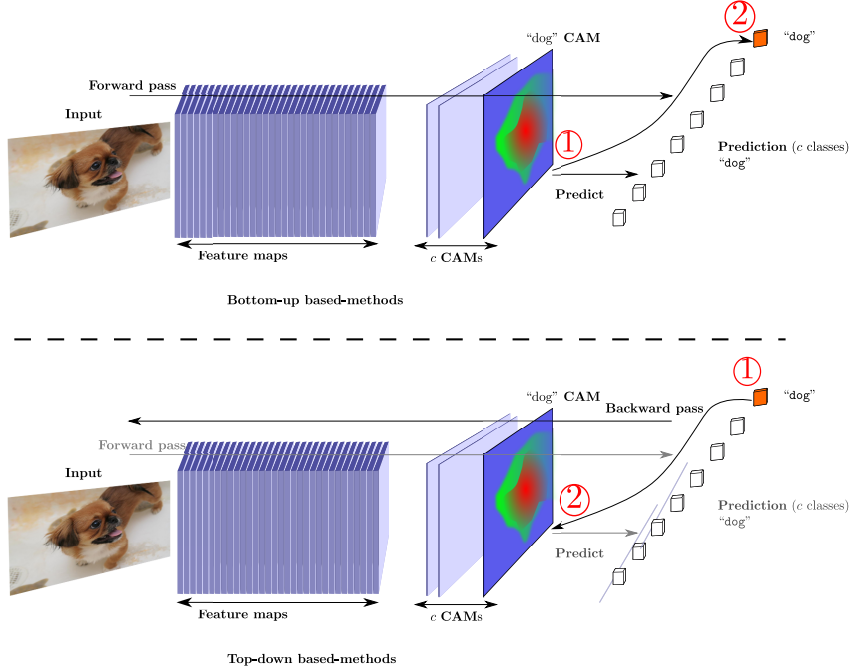


Figure 7: Illustration of the main difference between bottom-up (*top*) and top-down (*bottom*) WSL techniques. Both approaches provide CAMs, however, bottom-up techniques produce them during the forward pass, while top-down techniques require a forward, then a backward pass to obtain them.

(forward pass, Fig.7 (*top*)). Within this category, we identify two different subcategories of techniques to address weakly supervised localization. The first category contains techniques that are based on spatial pooling of either representations or scores which aims at classifying a bag of instances while obtaining localization throughout the activation of the spatial maps (i.e., classifying instances). The second category contains techniques related to object detection which essentially aim to detect regions associated with classes.

Methods based on spatial pooling. This category of techniques are mainly based on learning a spatial representation that promotes the localization of the objects of interest, and which is pooled to classify the input. Within this category, we distinguish two main strategies. • The first approach aims at building a global representation of the input and then classify it. This corresponds to the approach initially proposed by (Zhou et al., 2016) in which the global representation is obtained by averaging the local representations. The class-specific activations are then obtained by a linear combination of the features using the weight of the classification layer. This strategy has been widely used for natural scene images as well as for medical images (Feng et al.,

2017; Gondal et al., 2017; Izadyyazdanabadi et al., 2018; Sedai et al., 2018) where it often combines features from multiple levels (corresponding to different scales) to improve the performance. A more recent strategy proposed by (Ilse et al., 2018) builds a representation as a weighted sum of the local representations where the weights are attention scores produced by a scoring function. • The second approach aims at obtaining a global score for each class based on the local scores. The classification is done at the instance level and the scores are pooled using different strategies. The first approach proposed by (Oquab et al., 2015) uses max pooling to obtain a score for the image, while the final score for a class is the maximum score of all the instances. However, this pooling technique tends to focus on small discriminative parts of objects (Zhou et al., 2016). To alleviate this problem, (Pinheiro and Collobert, 2015b) propose to use a smoothed approximation of the max function to discover larger parts of the objects of interest. Finally, (Durand et al., 2017, 2016) propose to use negative evidence to obtain a global score: instead of using only the maximum scoring instances, the pooling is based on both the maximum and minimum scoring instances which provides a strong regularization during training. This method

has also been used in the medical field for histology image classification (Couture et al., 2018) and weakly supervised localization and image classification in the same type of images (Courtial et al., 2018).

Methods based on object detection. The second type of techniques within this category are related to Weakly Supervised Object Detectors (WSOD). The main goal of WSOD is to produce a region (or a set of regions) that are characteristic to one class (or a set of classes, not necessarily different). These regions are defined by rectangular bounding boxes and try to fit the object as much as possible (i.e., the outer edges of the object are in contact with the bounding box). The main difficulty of WSOD is to obtain an accurate placement of the bounding boxes. Most approaches rely on Region Proposal (RP) mechanisms such as Edge Boxes (Zitnick and Dollár, 2014) or Selective Search (Uijlings et al., 2013; Van de Sande et al., 2011). RP mechanism is used to generate a list of candidate regions that are likely to contain an object of interest. It can be introduced at different levels of the architecture and it has shown to impact the performance of the overall algorithm. An early approach using this mechanism is used in (Teh et al., 2016) where the content of each region is passed through an attention, then scoring modules to obtain an average image feature which is a weighted average of the proposals. (Bilen and Vedaldi, 2016) propose a WSOD framework to address the task of multi-class object detection. More improvement of this work has been proposed since then (Kantorov et al., 2016; Tang et al., 2017). Other approaches use multi-step training to first train a CNN for localization and then refine it for object detection (Diba et al., 2017; Ge et al., 2018; Sun et al., 2016). (Wan et al., 2018) propose to train a network to reduce its variance in terms of the proposals by reducing an entropy defined over the position of the proposals. (Shen et al., 2018) propose to use generative adversarial networks to generate the proposals.

3.1.2. Top-down weakly supervised localization techniques:

This second main category is based essentially on the backward pass information within a network to build an attention map in order to localize objects with respect to a selected class. The main idea in this category is based on an optimization algorithm that aims at maximizing the posterior response of the network given an output target (i.e., class). This op-

timization scheme allows building an activation map where neurons that support the output target are activated. Different approaches have been used to build these activation maps including a probabilistic Winner-Take-All process that combines bottom-up and top-down information to compute the winning probability of each neuron (Zhang et al., 2018a), a backward layer (Cao et al., 2015), or by computing the gradient of the output target with respect to the feature maps (Chattopadhyay et al., 2018; Selvaraju et al., 2017). In practice, these approaches are known to be computationally expensive; and the computation time and the required memory increase with the size of the image.

3.2. Description of bottom-up weakly supervised localization techniques:

Let us consider a set of training samples $\mathbb{D} = \{(\mathbf{x}^{(t)}, y^{(t)})\}$ of images $\mathbf{x}^{(t)} \in \mathbb{R}^{D \times H^{\text{in}} \times W^{\text{in}}}$ with H^{in} , W^{in} and D being the height, width and depth of the input image; and its image-level label (i.e., class) is $y^{(t)} \in \mathcal{Y}$ with C possible classes. For simplicity, we refer to the input and its label as (\mathbf{x}, y) .

The training procedure aims at learning a neural network that models the function $f_{\theta} : \mathbb{R}^{D \times H^{\text{in}} \times W^{\text{in}}} \rightarrow \mathcal{Y}$ where the input \mathbf{x} has an arbitrary height and width and θ is the network parameters. Typically, in a multi-class scenario, given an input, the network outputs a vector of scores $\mathbf{s} \in \mathbb{R}^C$ which is then normalized to obtain a posterior probability using a softmax function,

$$\Pr(y = i | \mathbf{x}) = \text{softmax}(\mathbf{s})_i = \frac{\exp(\mathbf{s}_i)}{\sum_{j=1}^C \exp(\mathbf{s}_j)}. \quad (1)$$

The predicted class is the one corresponding to the index of the maximum probability which is equivalent to taking the argmax of the score vector: $\underset{i}{\text{argmax}} \Pr(y = i | \mathbf{x}) = \underset{i}{\text{argmax}} \mathbf{s}_i$.

Beside the classification of the input image, we are interested in the localization of the object within the image as well. The network can output as well either a region of interest r related to the predicted class or a set of regions $\mathbb{R}_{\text{inter}} = \{r_i \mid i = 1, \dots, t\}$. The network can output as well a set of C activation maps of height H and width W to indicate the location of the object within each class. We note this set as a tensor of shape $\mathbf{M} \in \mathbb{R}^{C \times H \times W}$; where \mathbf{M}_c indicates the c^{th} map. \mathbf{M} is commonly referred to as *class activation maps* (CAM). In practice, and in most cases, the height and the width of the CAM

is *smaller* than the height and the width of the input image by a factor S called stride such that $H = H^{\text{in}}/S$ and $W = W^{\text{in}}/S$.

3.2.1. Bottom-up based-methods:

1) *Spatial pooling*. In this category, the beginning of the pipeline is usually the same for all techniques: a CNN extracts K feature maps $\mathbf{F} \in \mathbb{R}^{K \times H \times W}$, where K is the number of feature maps which is architecture-dependent. The feature maps \mathbf{F} are then used to compute a score per class using a spatial pooling either on the representation or the scores of the instances.

We can distinguish two main approaches to compute the per-class score: spatial representation pooling and spatial score pooling.

Spatial representation pooling. In this first approach, the feature maps produced by the CNN are spatially pooled to form a single representation $\mathbf{f} \in \mathbb{R}^K$ of the whole input, which is then classified.

Global average pooling (GAP). (Lin et al., 2013) propose a way of regularizing neural networks by adding GAP layers to avoid the use of fully connected layers that dramatically increase the number of parameters. The GAP module allows to obtain dense features $\mathbf{f} \in \mathbb{R}^K$ based on spatial features $\mathbf{F} \in \mathbb{R}^{K \times H \times W}$ by averaging the activations of each map,

$$\mathbf{f}_k = \frac{1}{H W} \sum_{i=1, j=1}^{H, W} \mathbf{F}_{k, i, j}, \quad (2)$$

where \mathbf{f}_k is the k^{th} feature of the output of the GAP. (Zhou et al., 2016) show that this pooling strategy can be used to obtain a localization ability in a CNN using only global labels. Typically, in a CNN, the last layer which classifies the representation \mathbf{f} is a fully connected layer parametrized by $\mathbf{W} \in \mathbb{R}^{C \times K}$ such that $\mathbf{s} = \mathbf{W}\mathbf{f}$ (bias is omitted for simplicity). The CAMs, denoted as $\mathbf{M} \in \mathbb{R}^{C \times H \times W}$, are then obtained using a weighted sum of the spatial feature \mathbf{F} ,

$$\mathbf{M}_c = \sum_{k=1}^K \mathbf{W}_{c, k} \mathbf{f}_k. \quad (3)$$

The main advantage of Eq.3 is that it does not depend on the size of the input. This technique has been used extensively in medical domain (Feng et al., 2017; Gondal et al., 2017; Izadyayazdanabadi et al., 2018; Sedai et al., 2018), often combined with a multi-level feature maps. Combining feature maps

from low layers within the network can allow to obtain CAM with high resolution and more precision. (Zhu et al., 2017) propose soft proposal networks (SPNs) which are based on (Zhou et al., 2016) with an extra module that generates a proposal map which highlights regions of the object in hand. Such proposal map is generated iteratively using random walk over a fully connected directed graph that connects each position within a feature map at a specific convolution layer. (Zhu et al., 2017) can be also categorized as an object detection method with region proposals (section 3.2.1).

(Zhang et al., 2018b) propose to build the CAMs \mathbf{M} by taking the maximum between two set of CAMs. The first set of CAMs is obtained in the same way as in (Zhou, 2017) and used to mask (or erase) a part of the feature maps based on thresholding. Using these masked features, a second set of CAMs is computed using a different layer. (Zhang et al., 2018b) argue that it makes a CNN discover relevant regions more effectively.

Attention-based deep MIL. (Ilse et al., 2018) propose to build an image (i.e., bag) representation using a weighted average of the instances representations based on an attention mechanism (Bahdanau et al., 2014). Given a set of features $\mathbf{F} \in \mathbb{R}^{K \times H \times W}$ extracted for an image, the representation \mathbf{f} of the image is computed as,

$$\mathbf{f} = \sum_{i=1, j=1}^{H, W} \mathbf{A}_{i, j} \mathbf{F}_{i, j}, \quad (4)$$

and $\mathbf{A}_{i, j} = \frac{\exp(\psi(\mathbf{F}_{i, j}))}{\sum_{i=1, j=1}^{H, W} \exp(\psi(\mathbf{F}_{i, j}))},$

Where $\mathbf{F}_{i, j}$ is (by an abuse of notation) the feature vector of the location (i.e., instance) indexed by i and j . $\psi : \mathbb{R}^K \rightarrow \mathbb{R}$ is a scoring function. The resulting representation \mathbf{f} is then classified by a fully connected layer. (Ilse et al., 2018) propose two scoring functions,

$$\psi_1(\mathbf{f}) = \mathbf{w} \tanh(\mathbf{V}\mathbf{f}), \quad (5)$$

$$\psi_2(\mathbf{f}) = \mathbf{w} [\tanh(\mathbf{V}\mathbf{f}) \odot \sigma(\mathbf{U}\mathbf{f})], \quad (6)$$

where $\mathbf{w} \in \mathbb{R}^L$ and $(\mathbf{V}, \mathbf{U}) \in \mathbb{R}^{L \times K}$ are learnable weights. This approach is designed specifically for binary classification and produces a matrix of attention weights $\mathbf{A} \in [0, 1]^{H \times W}$ with $\sum \mathbf{A} = 1$. This means that for a positive bag, negative instances should have an attention weight close to 0 while positive instances should have a high attention weights.

However, it is not possible to determine if an instance is actually predicted as positive or not except by fixing a threshold.

Spatial score pooling. In this second approach, the feature maps are used to produce the CAMs directly by classifying each instance. Then, the global per-class scores are obtained by pooling the instances' scores. The methods mainly differ by their strategy used to pool the instances' scores.

First, it is important to note that GAP (Zhou et al., 2016) is designed to be used when the last classification layer of a model is linear. The consequence is that the pooling can also be done on scores which is equivalent. With GAP, Eq.2, and Eq.3 allow to compute the per-class scores \mathbf{s}_c as,

$$\begin{aligned} \mathbf{s}_c &= \sum_{k=1}^K \mathbf{W}_{c,k} \mathbf{f}_k, \\ &= \frac{1}{HW} \sum_{k=1}^K \mathbf{W}_{c,k} \sum_{i=1,j=1}^{H,W} \mathbf{F}_{k,i,j}, \\ &= \frac{1}{HW} \sum_{i=1,j=1}^{H,W} \mathbf{M}_{c,i,j}, \end{aligned} \quad (7)$$

Eq.7 shows that the per-class score is computed by averaging the activations of the corresponding CAM. Instead of averaging the feature maps, taking the maximum value can be considered as well (Oquab et al., 2015). However, such an operation tends to favor small discriminative regions (Zhou et al., 2016). (Pinheiro and Collobert, 2015a; Sun et al., 2016) consider using an approximation to the maximum function (Boyd and Vandenberghe, 2004) as an alternative where the score of each map can be computed as,

$$\mathbf{s}_c = \frac{1}{q} \log \left[\frac{1}{HW} \sum_{i=1,j=1}^{H,W} \exp(q \mathbf{M}_{c,i,j}) \right], \quad (8)$$

where $q \in \mathbb{R}_+^*$ controls the smoothness of the approximation. A smaller value of q makes the approximation closer to the average function while a larger q makes it close to the maximum function. Thus, small values of q make the network consider large regions while large values consider only small regions.

Negative evidence mixing. (Durand et al., 2017, 2016) compute m feature maps per-class using 1×1 convolution. Then, compute their average to obtain

one feature map. While standard pooling methods are based on considering the maximum or the average of the activations within a map, (Durand et al., 2017, 2016) consider using both maximum and minimum activations. A maximum activation indicates a positive evidence of the presence of the corresponding object. In the other hand, a minimum activation indicates a negative evidence (Durand et al., 2015) of its presence. The benefits of such mixing of both information provides a regularization mechanism that prevents the model from overfitting compared to learning only from maximum activation for instance (Durand et al., 2017, 2016). Such pooling is computed over each map by considering the sum of the average of n^+ maximum activation and n^- of minimum activation. Specifically, the score for each class is computed as,

$$\mathbf{s}_c = \frac{Z_c^+}{n^+} + \alpha \frac{Z_c^-}{n^-}, \quad (9)$$

where Z_c^+ and Z_c^- correspond to the sum of the n^+ highest and n^- lowest activations of \mathbf{M}_c respectively and α is a hyper-parameter that controls the importance of the minimum scoring regions. Such an operation consists in selecting for each class the n^+ highest activation and the n^- lowest activation within the corresponding map. In medical domain, (Courtial et al., 2018) show the benefit of mixing negative evidence.

2) Object detection with region proposals. The second category of techniques relevant for weakly supervised localization is related to object detection. Many techniques have been proposed in order to find the coordinates of a relevant region using only image-level labels. The pipeline of these detectors usually contains three operations presented in Fig.8. The order of the operations of this pipeline can be changed to accommodate different strategies of supervision but the principle of the operations remains the same. In the next paragraphs, we describe some of the related work that is based on WSOD.

Attention networks for WSOD. In a similar manner to (Ilse et al., 2018), (Teh et al., 2016) propose to use a fully connected network to generate attention score for each instance. The initial region proposals are generated using the Edge Boxes (EB) (Zitnick and Dollár, 2014) on the input image. Then for each region, a feature vector representation is extracted using a pre-trained CNN. A fully connected network produces a score for each feature vector, which is

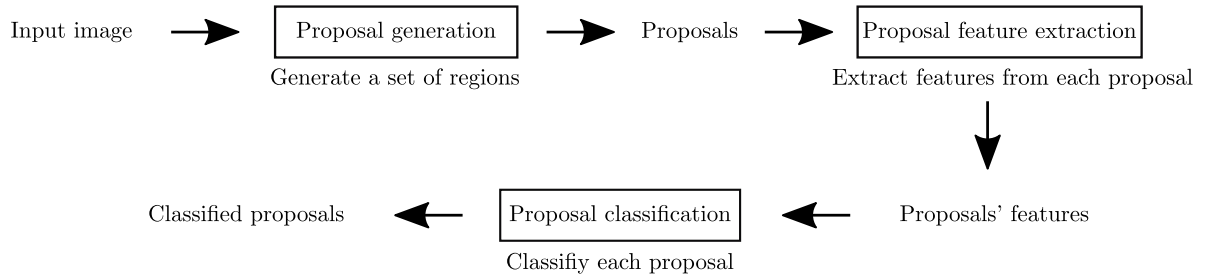


Figure 8: Standard pipeline for WSOD methods.

normalized using a softmax operation on the proposals. The image representation is the weighted sum of the feature vectors by the attention weights. The resulting representation is then classified by a fully connected layer. (Bency et al., 2016) propose an efficient way to extract top scoring regions from a CNN by performing a tree search on sub-regions of the feature maps. Given the feature maps produced by a CNN, four children regions of small size are extracted and each region is interpolated to produce a feature map of the same size as the parent. These four regions are classified by a fully connected layer. The top-scoring region for the class of the image then becomes the parent region. This process is iterated until it converges to a region with the maximum probability for the class of the image at train time.

Weakly supervised deep detection networks (WS-DDN). (Bilen and Vedaldi, 2016) is one of the approaches that has achieved an important improvement compared to previous WSOD techniques (Bilen et al., 2015, 2014; Cinbis et al., 2017; Wang et al., 2014). (Bilen and Vedaldi, 2016) propose a modified CNN architecture with two streams: one focusing on recognition and the other one on localization. In this approach, the proposals are generated from the input image using Selective Search (SS) (Uijlings et al., 2013; Van de Sande et al., 2011) or Edge Boxes (EB). In parallel, a CNN produces feature maps for the input image. A Spatial Pyramid Pooling (SPP) (He et al., 2014) is then used to extract the features corresponding to the region proposals from the feature maps. At this point, each region's features are processed by two different fully connected networks to produce classification scores $\mathbf{S}^{\text{class}} \in \mathbb{R}^{|\mathbb{R}_{\text{inter}}| \times C}$ and detection scores $\mathbf{S}^{\text{det}} \in \mathbb{R}^{|\mathbb{R}_{\text{inter}}| \times C}$. These scores are then normalized to obtain σ^{class} and σ^{det} using a

softmax function,

$$\sigma_{i,c}^{\text{class}} = \frac{\exp \mathbf{S}_{i,c}^{\text{class}}}{\sum_{j=1}^C \exp \mathbf{S}_{i,j}^{\text{class}}}, \quad (10)$$

$$\sigma_{i,c}^{\text{det}} = \frac{\exp \mathbf{S}_{i,c}^{\text{det}}}{\sum_{j=1}^C \exp \mathbf{S}_{i,j}^{\text{det}}}. \quad (11)$$

The final region-level scores $\mathbf{R} \in \mathbb{R}^{|\mathbb{R}_{\text{inter}}| \times C}$ are obtained throughout an element-wise product of the normalized classification and detection scores, and the per-class image-level scores are obtained by summing the region-level score for each class,

$$\mathbf{R} = \sigma^{\text{class}} \odot \sigma^{\text{det}}, \quad (12)$$

$$\text{and } \mathbf{s}_c = \sum_{i=1}^{|\mathbb{R}_{\text{inter}}|} \mathbf{R}_{i,c}. \quad (13)$$

(Kantorov et al., 2016) further improve this approach by adding more context information where \mathbf{S}^{det} becomes the combination of the score of a region and its surrounding (i.e., spatial context). This allows to obtain a better discrimination of the proposed region, eliminating regions that do not tightly fit an object.

Online instance classifier refinement. (Tang et al., 2017) propose another improvement of the WSDDN by refining the proposals multiple times based on the overlap of the proposals. When a proposal is a top-scoring region for a class that is present in the image, the refinement algorithm will look for all the other proposals that have a high overlap with it and set their label to one for this class. This process forces the model to gradually detect larger parts of objects as the training advances by fusing on high scoring and overlapping regions.

Weakly supervised region proposal network and object detection. (Tang et al., 2018) suggest that the proposal generation has a great influence on WSOD performance and can benefit from the feature maps

produced by a CNN instead of simply using SS or EB on the input image. Once the feature maps are obtained from the CNN, the proposals are generated in three steps. The first proposals are generated using a sliding window on the image. They are refined using the same principle as EB method. To further refine them, a fully connected network re-evaluates the objectness of the refined proposals. Finally, the different proposals are classified by extracting a feature vector representation using the same *region of interest* pooling algorithm as in Fast R-CNN (Girshick, 2015). This method presents the advantage of not relying on SS nor EB to generate the proposals which are known to be computationally expensive. *Region proposal filtering using top-down stream for multi-label recognition.* (Ge et al., 2018) propose to use multiple sources of information to obtain CAMs for better object detection. In this technique, the authors combine object heatmaps with top-down attention maps to obtain more accurate object instances. The object heatmaps are obtained using a pre-trained CNN, by adding the class probabilities of each proposal to its corresponding pixels when the class is present in the image. The attention maps are obtained using excitation backprop (Zhang et al., 2018a) on a second pre-trained CNN. Object heatmaps obtained in a feedforward manner are usually too smooth to give precise information on the object boundaries. Combining them with attention maps allows to better filter the region proposals, and reduce the number of false positive regions.

Deep self-taught learning. (Jie et al., 2017) suggest that training detectors with image-level supervision leads to poor-quality positive proposals. To start from good proposals, the authors propose to use a graph-based approach to refine the proposals initially generated by EB, by finding the dense sub-graph of proposals based on their spatial overlap. To improve the quality of the proposals, they propose to train a detector by *iteratively* selecting high-quality proposals based on their relative improvement compared to the previous training epoch. With this self-supervision, low-quality proposals obtain low improvement over the epochs, contrary to high-quality ones. This allows the detector to select high-quality regions.

Min-entropy latent model for WSOD. (Wan et al., 2018) suggest that there is an inconsistency between the weak supervision (absence of labels of object localization) and the learned objectives (i.e., asking the model to learn the object location) which

introduces randomness and uncertainty to object locations and object detectors. In order to decrease such uncertainty, the authors propose to minimize the entropy of a latent model which aims to reduce the variance of the proposals (i.e., the locations of the objects). The proposals are initially generated by SS and a feature representation is extracted for each proposal. They are further refined using a graph-based approach to fuse them when they present the high confidences for a class and a significant spatial overlap. Then, the model is trained to minimize the classification error on the most confident proposals. This produces sparse predictions on the most confident proposals which reduces the randomness of selected proposals during learning. *Generative adversarial networks for WSOD.* A main criticism of the WSOD techniques is that they usually follow a multi-step pipeline (Figure 8), leading to expensive computational cost, hence, a slow running time. (Shen et al., 2018) propose to improve the speed by training a WSOD within a generative adversarial framework. Three models are used in this approach: a generator G which is a one-stage detector (Liu et al., 2016) that outputs bounding boxes with associated probabilities, a discriminator D predicting the quality of bounding boxes for an image, and a surrogator F which is a modified version of WSDDN used to estimate image proposals. The intuition is that G , which is fast, will learn to generate the same proposals as F , which is slow in comparison, with the supervision of D . D learns to distinguish bounding boxes generated by G from accurate estimated ones generated by F .

3.3. Description of top-down weakly supervised localization techniques:

In this second main category, the weakly localization of objects is determined based on information obtained from the stream that goes from the output (top) toward the input (down). We can distinguish two related methods: backward based-methods, and gradient based-methods. We note that such approaches are computationally expensive compared to bottom-up methods (Sec.3.2.1).

Backward stream based-methods. Excitation backprop for top-down attention (Zhang et al., 2018a) is one of the illustrative examples of such approach. In its formulation, the authors propose a probabilistic winner-take-all formulation in the backward pass of the model to determine which units are active with respect to a selected output class. By

defining a prior distribution over the output classes, the winner neurons of low layer can be sampled recursively in a top-down fashion. Given a neuron a_z at some layer, its probability can be determined using the probability of its parent neurons $a_t \in \mathbb{P}_z$ at the previous layer as follows,

$$\Pr(a_z) = \sum_{a_t \in \mathbb{P}_z} \Pr(a_z|a_t) \Pr(a_t), \quad (14)$$

where $\Pr(a_z|a_t)$ is simply a normalized energy that flows from the neuron a_z to a_t with respect to all the neurons that share the same parent as a_z . Using such approach, it is possible to obtain a CAM at each convolutional layer. Since an image may contain many objects, the dominant neurons may belong to different classes. Thus, a CAM may contain the activations of more than one object. To deal with this, (Zhang et al., 2018a) propose a *contrastive* attention that builds a highly discriminative CAMs by keeping only one class and suppressing the rest. (Cao et al., 2015) propose a related work where an attention map is built with respect to a selected class using the backward information throughout a *feedback layer*. Neurons in feedback layers are updated iteratively to maximize the confidence of the output target. The selectivity in such neurons is controlled using a binary mask obtained throughout an optimization procedure.

Gradient based-methods. These approaches are based on computing the gradient of any output target with respect to the feature maps to determine the main locations that contribute to the prediction of the selected target. Such approaches are mainly used as *visual tools* to explain a network’s decision. (Selvaraju et al., 2017) is an illustrative example of this approach. In order to compute the CAMs, the authors propose to use GAP (Eq.3), where the coefficient of each feature map is computed using the gradient of the score of the selected target class with respect to that map. Therefore, a CAM for the class c is a linear combination of the feature maps, similar to Eq.3,

$$\mathbf{M}_c = \text{ReLU} \left(\sum_{k=1}^K \mathbf{A}_{c,k} \mathbf{F}_k \right), \quad (15)$$

$$\text{where } \mathbf{A}_{c,k} = \frac{1}{H W} \sum_{i=1, j=1}^{H, W} \frac{\partial s_c}{\partial \mathbf{F}_{k,i,j}}, \quad (16)$$

where s_c is the score for class c . This approach is a generalization of the the method proposed by (Zhou

et al., 2016) where the derivative of the score with respect to the feature map is used. In the case where the last classification is linear, both formulation are equivalent. This approach has been improved in (Chattopadhyay et al., 2018) to obtain better object localization, as well as explaining occurrences of multiple object instances in a single image.

3.4. A critical analysis:

Our first observation is that all the deep weakly supervised localization methods have been proposed and validated on natural scene images. Their application on histology images can be problematic due to the heterogeneous nature of these images. The second observation is that bottom-up techniques have attracted much more attention compared to top-down ones. A possible explanation to this is the simplicity of bottom-up methods which follows classical flow of information within a neural network. In contrast, top-down methods, which are inspired from human visual attention, are more complex in terms of implementation and inference. For these reasons, most of the techniques selected for our experimental evaluation are mainly from the bottom-up family.

Among bottom-up methods, we find weakly supervised localization methods based on a spatial pooling allowing localization of objects after being trained using global labels only. Often, this category of techniques is straightforward to use on histology images, and do not rely on any priors on the nature of the images at hand. Among the spatial pooling methods, we evaluate the work in (Zhou et al., 2016) which has shown promising results in terms of classification and weak localization. We consider using three different pooling techniques: average pooling, max pooling, and log-sum-exponential pooling (Eq.8), WILDCAT pooling (Durand et al., 2017) which has shown interesting results in terms of classification and object localization, and deep multi-instance learning (Deep MIL) (Ilse et al., 2018). All these methods have shown great potential for localization while maintaining high level of classification accuracy. The major drawback of these methods is that the resolution of the CAMs is small due the stride of the used backbone network. When pixel-level evaluation is required (typically to evaluate the Dice index), we interpolate the CAMs to match the input size using a bilinear interpolation.

Deep MIL method proposed by (Ilse et al., 2018) has two major limitations. Firstly, it is restricted to binary classification. Therefore, for datasets which

have more than two classes we adapt this method by replicating the pooling and scoring module to match the number of predicted classes. Secondly, this method produces attention scores for each instance which sum to 1. Therefore, when we evaluate at pixel-level, an instance is predicted as belonging to the positive class if its attention weight is superior to $\frac{1}{HW}$. We acknowledge that this is not a perfect criteria as edge cases are not covered: if all instances are predicted with the same score, all attention weights are equal to $\frac{1}{HW}$ which does not indicate whether the initial score was high (positive instance) or low (negative instance). However, we observe that this works well in practice, showing the potential of this method.

In bottom-up category, we also find WSOD techniques based on region proposals, mostly used for object detection. For our experiments, we use the work in (Tang et al., 2018) which shows a large improvement compared to other WSOD methods, and (Bilen and Vedaldi, 2016) which limits the use of SS or EB methods which are known to be computationally expensive. The main limitation presented in WSOD methods is that they are tailored to natural scene images. Therefore, most of them encode in their algorithms some priors on the object in such images. We recall that objects within natural scene images have usually a standard structure/shape, and they tend to be smooth; while a *cancerous region* within histology images, for instance, does not have any prior structure nor appearance. As a consequence of such adaptation for natural scene images, region proposal methods such as SS and EB rely on the fact that edges are likely to delimit an object and pixels inside an object are more likely to be similar. In histology images, the first fact is not clear to be true. Moreover, edges are expected to be very noisy due to high variation in the texture of the microscopic tissue and intensive presence of cell borders. For these reasons, we have not been able to obtain concluding results with WSOD methods despite our best efforts and therefore did not include them in our experiments.

For top-down methods, Grad-CAM and Average pooling are equivalent when the last layer (i.e., classification layer) of a model is linear. Since we use ResNet models in our study, this is always verified, meaning that both methods are equivalent. Therefore, we only report results for the Average pooling. We also initially wanted to evaluate Excitation Backprop (Zhang et al., 2018a) but we were not able to obtain a working code for this method using the

PyTorch framework.

4. Experimental methodology

In this section, we present an experimental evaluation of several deep weakly supervised localization methods from the previous section that are relevant in histology image analysis. The aim of our experiments is to show the ability of selected methods to correctly classify histology images, and localize cancer regions of interest. The experiments are conducted on four public datasets of histology images which are described in Sec.4.1. Most of the public datasets were made exclusively for classification or segmentation purpose (Daisuke and Shumpei, 2018). There are extremely rare datasets that have image-level and pixel-level annotation simultaneously. The only dataset that we found that has both types of annotation is GlaS (Sec.4.1.3) which is not enough for our evaluation. For this reason, we went further and create a dataset with the required annotations by sampling patches from WSIs from CAMELYON16 dataset (Sec.4.1.4) using a concise protocol (Sec.4.2.3). Sec.4.3 provides a brief description of the training setup of the relevant techniques that we selected in our comparative study.

4.1. Datasets:

We describe in this section the four public datasets of histology images that we have used in our experiments. A brief description of the datasets is presented in Tab.1.

4.1.1. BreaKHis dataset:

BreaKHis is a publicly available⁷ dataset for microscopic biopsy images of benign and malignant breast tumor (Spanhol et al., 2016b). The images were collected through a clinical study from January 2014 to December 2014, to which all patients referred to the P&D Laboratory⁸ with a clinical indication of breast cancer were invited to participate. The institutional review board approved the study and all patients provided their written consent. All the data were anonymized. Samples were generated from the breast tissue biopsy slides, stained with H&E. The samples were collected by surgical open

⁷<https://web.inf.ufpr.br/vri/databases/breast-cancer-histopathological-database-breakhis>

⁸Pathological Anatomy and Cytopathology, Parana, Brazil: [http://www.prevencaoedиagnose.com.br](http://www.prevencaoediagnose.com.br)

Table 1: Brief description of the used datasets in our experiments. (seg.: segmentation.)

Dataset	Medical aspect	Type of image	#Images	Number of classes	Image-level labels	Pixel-level labels
BreakHis	Breast cancer	Patches	7, 909	2 classes: benign, malignant.	Yes	No
BACH (Part A)	Breast cancer	Patches	400	4 classes: normal, benign, in Situ, invasive	Yes	No
GlaS	Colon cancer	Patches	165	2 classes: benign, malignant	Yes	Yes (gland seg.)
CAMELYON16	Cancer metastases in Lymph Nodes	WSIs	399	2 classes: normal, metastases	Yes	Yes (tumor seg.)

biopsy, prepared for histological study and labeled by pathologists of the P&D Lab. The diagnosis of each case was produced by experienced pathologists and confirmed by complementary exams such as immunohistochemistry analysis.

The original images were acquired in three-channel red-green-blue color space (RGB, 24-bit color depth, 8 bit per channel), with resolution of 752×582 using magnifying factors of $40\times$, $100\times$, $200\times$, and $400\times$. The images were then cropped into size 700×460 and saved in portable network graphics format (PNG) with no compression, nor normalization, nor color standardization. Fig.9 shows these four magnification facts on a single image. Up to date, the dataset is composed of 7,909 images divided into benign and malignant tumors. Tab.2 summarizes the dataset distribution in terms of number of images per class, magnification factor, and patient. The classes benign and malignant are subdivided into different categories. However, in our experiments, we limit ourselves to the two main classes, i.e., benign against malignant. For more details on the dataset, we refer to (Spanhol et al., 2016b).

Table 2: BreakHis dataset (Spanhol et al., 2016b) distribution by class, magnification factor, and patient.

Magnification	Benign	Malignant	Total
$40\times$	625	1,370	1,995
$100\times$	644	1,437	2,081
$200\times$	623	1,390	2,013
$400\times$	588	1,232	1,820
Total	2480	5,429	7,909
#Patients	24	58	82

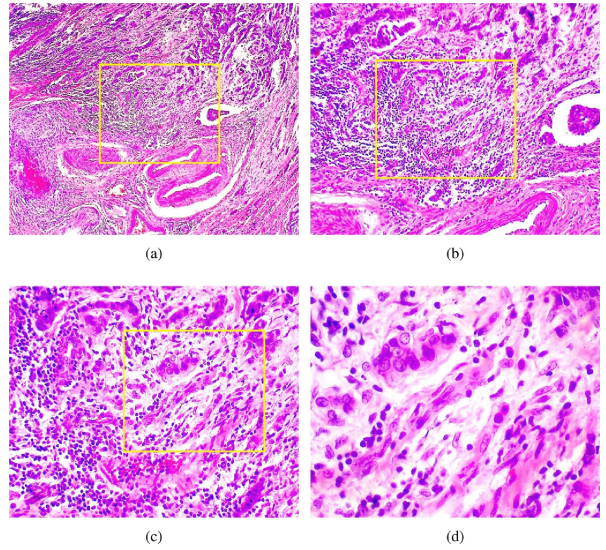


Figure 9: Slides of breast malignant tumor (stained with H&E) seen in different magnification factors: (a) $40\times$, (b) $100\times$, (c) $200\times$, and (d) $400\times$. Highlighted rectangle, which is manually added for illustration purposes only, is the area of interest selected by pathologist to be detailed in the next higher magnification factor (Credit: (Sudharshan et al., 2019)).

4.1.2. BACH challenge dataset (Part A) 2018:

The Grand Challenge on BreAst Cancer Histology images (BACH)⁹ (Aresta et al., 2018), which is a follow-up of the Bioimaging challenge of 2015¹⁰, was organized in 2018 in the aim of advancing state-of-the-art in automatic classification of histology images. A large annotated dataset of H&E stained breast histology images, composed of both microscopy and Whole Slide Images, was specifically compiled and made publicly available for the challenge. The challenge is composed of two parts. Part A is based on the microscopy images and dedicated for image classification task, while Part B is based

⁹<https://iciar2018-challenge.grand-challenge.org/>

¹⁰http://www.bioimaging2015.ineb.up.pt/challenge_overview.html

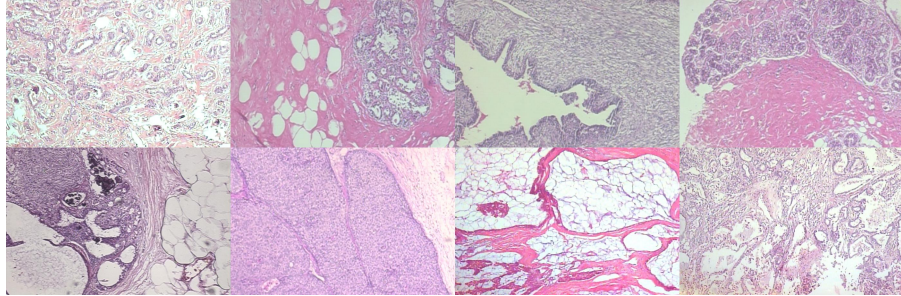


Figure 10: Samples from test set of fold 1 (Spanhol et al., 2016a) from BreaKHis dataset. *Row 1: Benign. Row 2: Malignant.*

on WSI and considered for image segmentation task. In our experiments, we consider only Part A since working directly on WSIs adds a heavy complexity to the learning algorithms in term of memory and running time (Sec.2.3).

The microscopy dataset is composed of 400 training images and 100 test images distributed evenly between four classes (image level labels): normal, benign, in Situ, and invasive. Fig.11 illustrates some examples from different classes. All images were acquired in 2014, 2015, and 2017 using Leica DM 2000 LED microscope and Leica ICC50 HD camera. All patients are from the Covilhã and Porto regions (Portugal). The annotation was performed by two medical experts. Images where there was disagreement between the normal and benign classes were discarded. The remaining doubtful cases were confirmed via immunohistochemical analysis. The provided images are in RGB Tagged Image File Format (TIFF). All the images have the same size (2,048, 1,536) pixels and a pixel scale of $(0.42\mu m, 0.42\mu m)$. (Areata et al., 2018) provide more details on the challenge and the provided data.

In our experiments, we consider a classification task with the four classes of the dataset. The challenge made public images of the train and test sets. However, only train labels are provided. A model prediction must be uploaded to the website of the challenge for evaluation on the test set. Only three trials are allowed per day. Therefore, we limit ourselves to use only the train set for training and evaluation using a cross-validation scheme. We take half of the samples of each class to build the test set, while we apply k -fold over the left samples to build the validation and train set.

4.1.3. GlaS dataset:

Colorectal adenocarcinoma originating in intestinal glandular structures is the most common form

of colon cancer (Sirinukunwattana et al., 2017). The morphology of intestinal glands, including architectural appearance and glandular formation is used in clinical practice by pathologists to inform prognosis and plan treatment of individual patients. Achieving good inter-observer as well intra-observer reproducibility of cancer grading is a major challenge in the pathology domain. The Gland Segmentation in Colon Histology Images Challenge Contest¹¹ (Sirinukunwattana et al., 2017) was held in 2015 in the aim to advance automated approaches for quantifying the morphology of glands.

The challenge provides a dataset, GlaS, composed of 165 images derived from 16 H&E histological sections of two grades (classes): benign, and malignant (Fig.12). The digitization of these histological sections into WSI was accomplished using a Zeiss MIRAX MIDI Slide Scanner with a pixel resolution of $0.465\mu m$. The WSI were subsequently rescaled to a pixel resolution of $0.620\mu m$ (equivalent to $20\times$ objective magnification). Tab.3 summarizes the partitioning of the dataset with the images size details. (Sirinukunwattana et al., 2017) provide more information on the dataset.

Since the challenge was primarily made for segmentation, a ground truth of the glandes segmentation is provided (pixel-level annotation). Aside the segmentation labels, image-level labels are also provided with two classes: benign, or malignant.

In this dataset, the glandes are the regions of interest that the pathologists use to prognosis the image grading of being benign or malignant. Therefore, in our later experiments (Sec.5), we are interested in measuring how well the model relies on such medically-valid regions of interest to predict the global class of the image. Therefore, the localized regions by the model are considered as a visual inter-

¹¹<https://warwick.ac.uk/fac/sci/dcs/research/tia/glascontest>

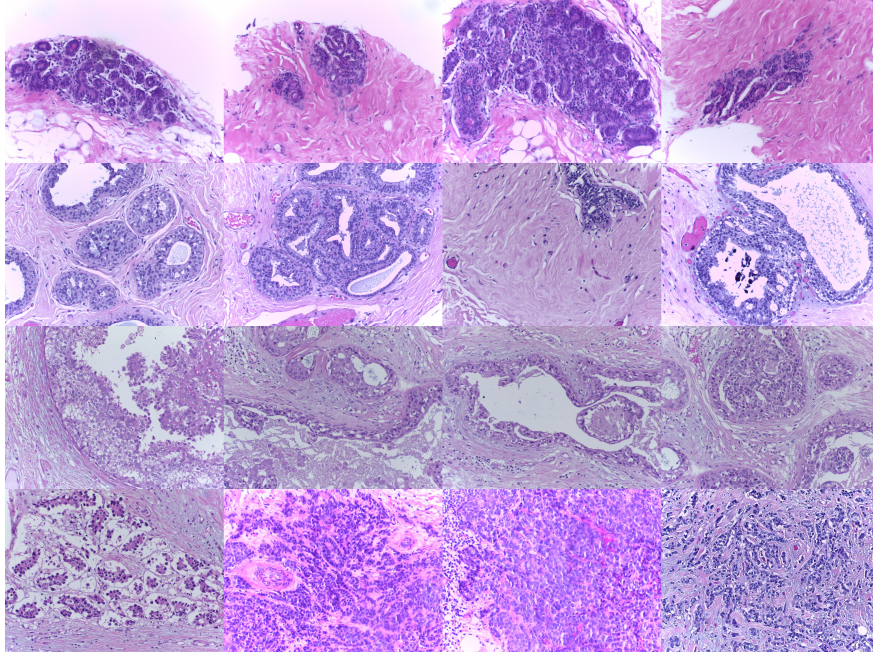


Figure 11: Samples from BACH public train dataset. *Row 1*: Normal. *Row 2*: Benign. *Row 3*: In Situ. *Row 4*: Invasive.

prebability tool to justify the model’s decision. We note that only image-level labels are used during the training, while pixel-level labels are used to evaluate the accuracy of localizing regions of interest (i.e., glandes). In our experiments, Test Part A, B are mixed (Tab.3).

Table 3: Details of the GlaS dataset (Sirinukunwattana et al., 2017).

Histologic Grade	Number of Images ((Width, Height) in Pixels)		
	Training Part	Test Part A	Test Part B
Benign	37 $\begin{cases} 1 & (574, 433) \\ 1 & (589, 453) \\ 35 & (775, 522) \end{cases}$	33 $\begin{cases} 1 & (574, 433) \\ 4 & (589, 453) \\ 28 & (775, 522) \end{cases}$	4 (775, 522)
Malignant	48 $\begin{cases} 1 & (567, 430) \\ 3 & (589, 453) \\ 44 & (775, 522) \end{cases}$	27 $\begin{cases} 1 & (578, 433) \\ 2 & (581, 442) \\ 24 & (775, 522) \end{cases}$	16 (775, 522)

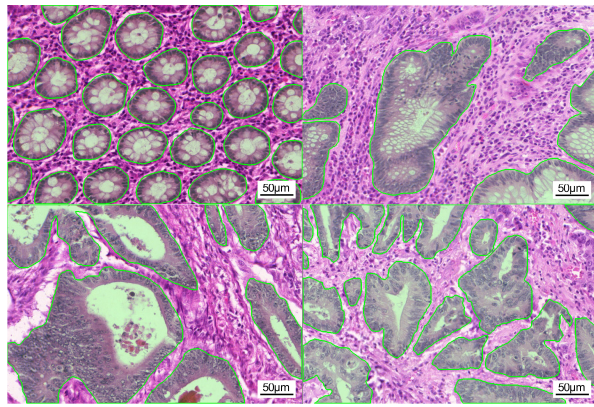


Figure 12: Example of images of different classes with their segmentation from GlaS dataset (Credit: (Sirinukunwattana et al., 2017)). *Row 1*: Benign. *Row 2*: Malignant.

4.1.4. CAMELYON16 dataset:

The Cancer Metastases in Lymph Nodes Challenge 2016 (CAMELYON16)¹² competition (Ehteshami Bejnordi et al., 2017) was organized to investigate the potential of machine learning algorithms for detection of metastases in H&E stained tissue sections of sentinel auxiliary lymph nodes (SNLs) of women with breast cancer.

The organizers of the challenge collected 399 WSIs of SNLs during the first half of 2015. SNLs were retrospectively sampled from 399 patients that underwent surgery for breast cancer at 2 hospitals in the Netherlands: Radboud University Medical Center (RUMC) and University Medical Cen-

¹²<https://camelyon16.grand-challenge.org/Home>

ter Utrecht (UMCU). The need for informed consent was waived by the institutional review board of RUMC. The WSIs were acquired at two different centers using two different scanners. RUMC images were produced with a digital slide scanner (Pannoramic 250 Flash II; 3DHISTECH) with a $20\times$ objective lens (specimen-level pixel size, $0.243\mu\text{m} \times 0.243\mu\text{m}$). UMCU images were produced using a digital slide scanner (NanoZoomer-XR Digital slide scanner C12000-01; Hamamatsu Photonics) with a $40\times$ objective lens (specimen-level pixel size, $0.226\mu\text{m} \times 0.226\mu\text{m}$). The WSIs are annotated globally to normal or metastases. The WSIs with metastases are further annotated at pixel-level to indicate regions of tumors. The annotations were first drawn by two students (one from each hospital), and then every slide was checked in details by one of the two expert pathologists (one from RUMC and the second from UMCU). In case of uncertainty, pathologist opt to use immunohistochemistry to resolve the diagnostic. An example of a WSI is provided in Fig.13. Among the provided 399 WSIs, 270 are used for training (111, 159 with and without nodal metastases), and 129 for test (49, 80 with and without nodal metastases)¹³. (Ehteshami Bejnordi et al., 2017) provide more details on the dataset, the challenge, and its final results.

Two tasks were defined in the challenge: identification of individual metastases in WSIs (task 1), and classification of every WSI as either containing or lacking SNL metastases (task 2). The WSIs are extremely large (many gigabytes per image and a resolution of $100,000^2$ pixels for each image) which makes it inconvenient to conduct our experiments for the purposes of this survey. Therefore, we consider neither of the two tasks. However, we design a concise protocol to assess the different models' capacity in localizing regions of interest (Sec.4.2). Our protocol consists in building a weakly supervised learning scenario for object localization through a binary classification task (normal against metastases) where we have both pixel-level and image-level labels and only image-level labels are used for training. In order to build train, validation, and test sets, we sample a set of patches from the WSIs where a patch is given an image-level label of metastases or normal depending if it contains cancerous pixels or not. If it is a metastatic patch, a binary mask that indicates

the cancerous pixels is constructed based on the WSI pixel-level annotation.

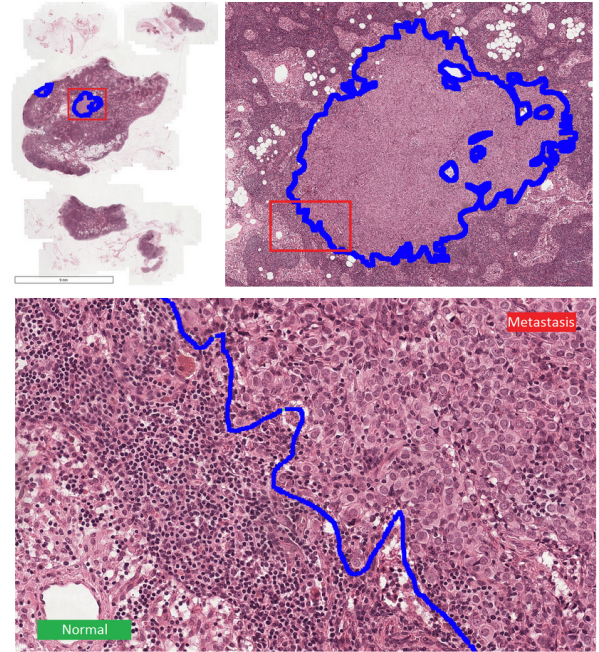


Figure 13: Example of metastatic regions in a WSI from CAMELYON16 dataset (Credit: (Sirinukunwattana et al., 2017)). *Top left*: WSI with tumor. *Top right*: Zoom to one of the metastatic regions. *Bottom*: Further zoom into the frontier between normal and metastatic regions.

4.2. Experimental protocol:

4.2.1. Performance metrics:

We define in this section our evaluation metrics. In this survey, we are interested in evaluating a model's capacity to correctly classify an image, and, as well as correctly localizing regions of interest. To this end, we consider two types of evaluation:

Evaluation A. In this evaluation setup we focus only on a model's performance in term of classification. As evaluation metric, we consider using the accuracy measure,

$$\text{accuracy} = 100 \frac{\#\text{correctly classified samples}}{\#\text{samples}} (\%) , \quad (17)$$

where $\#\text{correctly classified samples}$ is the total number of correctly classified samples, and $\#\text{samples}$ is the total number of samples; and the mean Average Precision measure (Su et al., 2015) (mAP),

$$\text{mAP} = \frac{1}{c} \sum_{k=1}^c \text{AP}_k 100 (\%) , \quad (18)$$

¹³Sample **test_114** is discarded since the pixel level annotation was not provided. Therefore, the test set is composed of 128 samples with 48 samples with nodal metastases.

where c is the total number of classes, and AP_k is the average prevision of the class k . A perfect model has 100% accuracy and 100% mAP. In this setup, all the relevant models are evaluated on the BreaKHis (Spanhol et al., 2016b) and BACH (Part A) (Aresta et al., 2018) datasets. The image-level labels are the only required supervised annotation for the training and evaluation of the models.

Evaluation B. In this evaluation setup we focus mainly on the performance of a model in term of localizing regions of interest –i.e., localization performance at pixel level–. To this end, we rely on standard segmentation metrics. In our experiments, we consider Dice index metric (Dice, 1945) which is a measure of agreement or similarity between two sets of samples. Give \mathbb{G} a set of pixels belonging to a ground truth object, and \mathbb{S} , a set of pixels belonging to a segmented object. Dice index is defined as follows,

$$\text{Dice}(\mathbb{G}, \mathbb{S}) = \frac{2|\mathbb{G} \cap \mathbb{S}|}{|\mathbb{G}| + |\mathbb{S}|}, \quad (19)$$

where $|\cdot|$ denotes set cardinality, $\mathbb{G} \cap \mathbb{S}$ is the set of overlapped pixels between \mathbb{G} and \mathbb{S} . Dice index ranges in the interval $[0, 1]$, where the higher the value, the more concordant the segmentation and the ground truth. A Dice index of 1 indicates a perfect segmentation. To compute the Dice index, the pixel-level annotation is required. In the context of evaluating weakly supervised localization models, such annotation is exclusively used for evaluation –i.e., it is not used for training–. Only image-level annotation is used for training. GlaS (Sirinukunwattana et al., 2017), and a variant of CAMELYON16 (Ehteshami Bejnordi et al., 2017) (Sec.4.2.3) datasets are used for this evaluation. Classification performance at image-level is reported as well.

The aim of this type of evaluation is to measure how well a model, that is trained a weakly supervised localization task –i.e., using only image-level annotation and deprived from pixel-level annotation–, can localize regions of interest that practically require pixel-level supervision. Such weakly supervised models are compared with an ideal model that is trained for segmentation only using pixel-level annotation without image-level annotation –i.e., segmentation task–. In this context, we consider using the model U-Net (Ronneberger et al., 2015) which is a reference model in medical image segmentation. Such model is trained exclusively on pixel-level annotation: In the case of GlaS we train the model to segment the

glands; while in the case of CAMELYON16 we train it to segment cancerous regions.

We note that in the case of the GlaS dataset (Sec.4.1.3), and the case of weakly supervised model that outputs two features maps to indicate regions of interest, Dice index is computed using the heat map corresponding to the true image-level label. In the case of CAMELYON16 dataset (Sec.4.1.4), Dice index is computed with respect to the heat map that corresponds to the metastatic class. This implies that we perform the evaluation only on the samples with metastatic image-level label.

4.2.2. Datasets split:

In our experiments, the test set is fixed in all the datasets, and only train and validation sets are changed using a k -fold scheme. The only exception to the fixed test set rule is BreakHis where we use the provided folding (Spanhol et al., 2016a) where each fold, and each magnification has its own test set. However, we apply the k -fold over the provided train set to obtain the train and validation sets. In our experiments, given the provided train set, we take 20% of the samples for validation, and 80% for actual training. This leads to 5-folds partitioning. We report the average of the mean and the standard deviation of each metric over the trials in the following form: mean \pm standard deviation. We note that BreaKHis and BACH (Part A) datasets are used for **Evaluation A** (Sec.4.2.1) while GlaS and CAMELYON16 are used for **Evaluation B** (Sec.4.2.1). The results of our experiments on BreaKHis, BACH (Part A), GlaS, and CAMELYON16 are presented in Tab.5, Tab.6, Tab.7, and Tab.8/Tab.9, respectively. We note that in order to compute Dice index for a set, we average Dice index of each image, unless stated otherwise.

The used deterministic code for creating the folds of all the datasets, sampling from CAMELYON16, the coordinates of the sampled patches from CAMELYON16, and the code of all the experiments is publicly available¹⁴.

In the next section, we describe the experimental protocol that we used to create a weakly supervised localization scenario from CAMELYON16 dataset.

4.2.3. CAMELYON16 weakly supervised localization protocol:

We describe in this section our protocol of creating a weakly supervised localization dataset

¹⁴https://github.com/jeromerony/survey_wsl_histology

from CAMELYON16 dataset (Ehteshami Bejnordi et al., 2017). Samples are patches sampled from WSIs. Each patch has two levels of annotation:

- Image-level label y : the class of the patch, where $y \in \{\text{normal}, \text{metastatic}\}$. This annotation is provided for all patches.
- Pixel-level label $\mathbf{Y} = \{0, 1\}^{H^{\text{in}} \times W^{\text{in}}}$: a binary mask where the value 1 indicates a **metastatic** pixel, and 0 a **normal** pixel. For **normal** patches, this mask will contain 0 only.

First, we split CAMELYON16 dataset into train, validation, and test set at *WSI-level* as described in Sec.4.2.1. This prevent patches from the same WSI to end up in different sets. All patches are sampled with the highest resolution from WSI –i.e., level = 0 in WSI terminology–. We present in the following our methodology of sampling metastatic and normal patches.

Sampling metastatic patches. Metastatic patches are sampled only from metastatic WSIs around the cancerous regions. Sampled patches will have image-level label, and a pixel-level label. The sampling follows these steps: 1. Consider a metastatic WSI. 2. Sample a patch \mathbf{x} with size (H, W) . 3. Binarize the patch into \mathbf{x}^b mask using OTSU method (Otsu, 1979). Pixels with value 1 indicate tissue. 4. Let $p_t^{\mathbf{x}^b}$ be the tissue percentage within \mathbf{x}^b . If $p_t^{\mathbf{x}^b} < p_t$, discard the patch. 5. Compute the metastatic binary mask \mathbf{Y} of the patch \mathbf{x} using the pixel-level annotation of the WSI (values of 1 indicate a metastatic pixel). 6. Compute the percentage $p_m^{\mathbf{x}}$ of metastatic pixels within \mathbf{Y} . 7. If $p_m^{\mathbf{x}} < p_0$, discard the patch. Else, keep the patch \mathbf{x} and set $y = \text{metastatic}$ and \mathbf{Y} is its pixel-level annotation.

We note that we sample *all* possible metastatic patches from CAMELYON16 using the above approach. Sampling using such approach will lead to a large number of metastatic patches with high percentage of cancerous pixels (patches sampled from the center of the cancerous regions). These patches will have their binary annotation mask \mathbf{Y} full of 1. Using these patches will shadow the performance measure of localization of cancerous regions. To avoid this issue, we propose to perform a calibration of the sampled patches in order to get rid of most of such patches. We define two categories of metastatic patches:

1. **Category 1:** Contains patches with $p_0 \leq p_m^{\mathbf{x}} \leq p_1$. Such patches are rare, and contain only small region of cancerous pixels. They are often located at the edge of the cancerous

regions within a WSI.

2. **Category 2:** Contains patches with $p_m^{\mathbf{x}} > p_1$. Such patches are extremely abundant, and contain a very large region of cancerous pixels (most of the time the entire patch is cancerous). Such patches are often located inside the cancerous regions within a WSI.

Our calibration method consists in keeping all patches within **Category 1** and throwing most of the patches in **Category 2**. To this end, we apply the following sampling approach:

1. Assume we have n patches in **Category 1**. We will sample $n p_n$ patches from **Category 2**, where p_n is a pre-defined percentage.
2. Compute the histogram of the frequency of the percentage of cancerous pixels within all patches. Assuming a histogram with b bins.
3. Among all the bins with $p_m^{\mathbf{x}} > p_1$, pick uniformly a bin.
4. Pick uniformly a patch within that bin.

This procedure is repeated until we sample $n p_n$ patches from **Category 2**. Tab.4 presents the number of sampled patches from the entire CAMELYON16 dataset, before and after calibration. We note that the sampling of metastatic patches is done separately on the original provided train, and test sets of WSIs.

In our experiments, patches are not overlapping. We use the following configuration: $p_0 = 20\%$, $p_1 = 50\%$, $p_t = 10\%$, $p_n = 1\%$. The number of bins in the histogram is obtained by dividing the interval $[0, 1]$ with a delta of 0.05. We investigate the following patch sizes: (512, 512), (768, 768) and (1024, 1024). In one experiment, only one patch size is used –i.e., patches with different sizes are not mixed within the same set–. Fig.14 illustrates an example of metastatic patches and their corresponding masks.

We note that metastatic patches are sampled then calibrated only once from the original train, and test WSI. Therefore, each WSI has a *unique* and *unchanged* set of metastatic patches.

Table 4: Total number of metastatic patches sampled from the entire CAMELYON16 dataset (Ehteshami Bejnordi et al., 2017) using our sampling approach; and different patch sizes. Patches are not overlapping.

Patch size	#Patches: Before calibration			#Patches: After calibration		
	Total	$p_0 \leq p_m^{\mathbf{x}} \leq p_1$	$p_m^{\mathbf{x}} > p_1$	Total	$p_m^{\mathbf{x}} > p_1$	
(512, 512)	137,769	14,912	122,857	24,435	9,523	
(768, 768)	64,127	9,512	54,615	15,377	5,865	
(1,024, 1,024)	37,598	6,988	30,610	11,470	4,482	

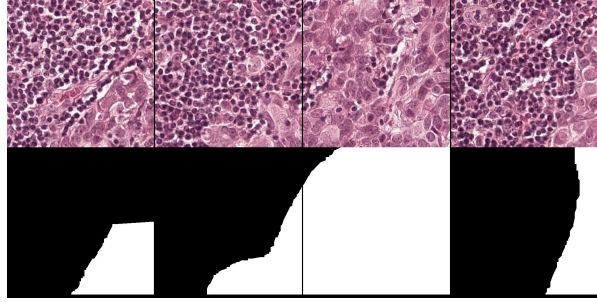


Figure 14: Example of metastatic patches with size (512, 512) sampled from CAMELYON16 dataset (WSI: `tumor_001.tif`). *Top row*: Patches. *Bottom row*: Masks of metastatic regions (white color).

Sampling normal patches. Normal patches are sampled only from normal WSI. A normal patch is sampled randomly and uniformly from the WSI (without repetition nor overlapping). If the patch has enough tissue ($p_t^{\text{b}} \geq p_t$), the patch is accepted. The measure of tissue mass is performed at level = 6 where it is easy for the OTSU binarization method to split the tissue from the background. We double-check the tissue mass at level = 0.

Let us consider a set (train, validation, or test) at patch level within a specific fold. We first pick the corresponding metastatic patches from the metastatic WSI, assuming n_m is their total number. Assuming there is h normal WSIs in this set, we sample the same number of normal patches as the total number of metastatic ones. In order to mix the patches from all the normal WSI, we sample $\frac{n_m}{h}$ normal patches per normal WSI. In our experiment, we use the same setup as in the case of sampling metastatic patches: $p_t = 10\%$. Fig.15 illustrates an example of normal patches. This sampling procedure implies that metastatic patches are fix in all the metastatic WSI (also, they are the same across folds), while normal patches within a normal WSI change across folds.

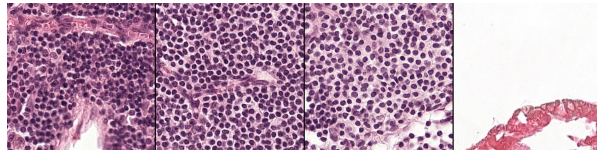


Figure 15: Example of normal patches with size (512, 512) sampled from CAMELYON16 dataset (WSI: `normal_001.tif`).

4.3. Training setup:

We present in this section the training setup that we used in our experiments for both learning methods: weakly supervised, and fully supervised training.

4.3.1. Weakly supervised training:

For all methods, we use an ImageNet-pretrained ResNet-18 (He et al., 2016) architecture as a feature extractor. The optimization algorithm used is Stochastic Gradient Descent (SGD) with Nesterov acceleration with a momentum of 0.9 and a weight decay of 0.0001. The learning rate is set to 0.01 for the first half of the training and decayed to 0.001 for the second half. The minibatch size is set to 64 for all datasets except GlaS where it is set to 32. For all datasets, we randomly flip the images during training. We also perform random color jittering on the images with parameters brightness, contrast and saturation at 0.5 and hue at 0.05 (from the PyTorch¹⁵ framework).

To train models using minibatches, we need to have images of the same size in a minibatch. Since the images have different sizes between datasets and within some datasets, the cropping and resizing strategies differ between datasets. Even though we may use only a part of an image to train, the cropped patch inherits the same label of the entire image.

For BACH dataset, the image size is large (2048, 1536). Therefore, we train on patches extracted from the images rather than on the full images; and each patch receive the image label. The extracted patches have a size of (512, 512) at random locations and random rotations while ensuring that no empty zone is included (which happens when sampling too close to the borders of the image depending on the angle of rotation). We train all the models during 20 epochs. For the BreakHis and GlaS datasets, we extract patches of size (448, 448) and (416, 416) respectively at random locations and rotate them with a random angle in $\{0^\circ, 90^\circ, 180^\circ, 270^\circ\}$. For the BreakHis dataset, the models are trained during 80 epochs and for GlaS dataset, they are trained for 160 epochs since the number of samples is very small. For CAMELYON16 dataset, the images are simply rotated with a random angle in $\{0^\circ, 90^\circ, 180^\circ, 270^\circ\}$. The models are trained for 20 epochs.

¹⁵<https://pytorch.org>

In the case of the LSE and WILDCAT pooling, the hyper-parameters are chosen depending on the recommended values in their original papers. For the LSE pooling, we use $q = 10$. For WILDCAT, we set n^+ and n^- to correspond to 10% of highest and lowest scoring instances each and $\alpha = 0.6$.

For BreakHis and BACH datasets, we also study the impact of the number of training samples by training with only a fraction of each dataset. For both datasets, we do not change the size of the validation set nor the test set. To reduce the size of the training set, we randomly sample a given fraction of the examples in each class to keep the same balance between the classes. For BACH, we use the following percentages: 10%, 25%, 50%, 75%, 100% which corresponds to the following number of training samples *per class*: 4, 10, 20, 30, 40, respectively. For BreakHis, we use the following percentages: 4%, 10%, 25%, 50%, 75%, 100%. Since each magnification has a different number of samples, and for clarity, we prefer to not mention the per class number of samples. However, they can be easily computed based on Tab.2.

4.3.2. Fully supervised training:

We also train a fully supervised U-Net architecture (Ronneberger et al., 2015) on GlaS and CAMELYON16 datasets to obtain an upper bound performance in term of localization in a fully supervised setting. For both datasets, we train using SGD with Nesterov acceleration with a momentum of 0.9 and a weight decay of 0.0001. The learning rate is set to 0.1 and decayed during training depending on the number of epochs to reach 0.001 at the end of the training. For both datasets, the minibatch size is set to 16.

For GlaS dataset, the model is trained for 960 epochs and the learning rate is divided by 10 every 320 epochs. For CAMELYON16 dataset, the model is trained for 90 epochs and the learning rate is divided by 10 every 30 epochs. We use the same augmentations as in the weakly-supervised training for both datasets (Sec.4.3.1).

5. Results, interpretation, and future directions

5.1. Evaluation A – classification performance:

Tab.5, 6, 7, 8 present the obtained results in term of classification performance for the different models on the four datasets in term of accuracy and average

precision (AP) or mean average precision (mAP) in the case of a multi-class dataset. For this evaluation, the performance of Grad-CAM is not reported since the method is identical to CAM for classification.

We observe that all the studied methods achieved similar high classification performance on GlaS (Tab.7) and CAMELYON16 (Tab.8) datasets ($\sim 100\%$) with low variation. This may suggest that both datasets are easy for a classification task. For BreakHis (Tab.5) and BACH (Tab.6), we observe that the classification performance is high and similar for CAM, WILDCAT and Deep MIL (even adapted to the multi-class scenario) and low for LSE and Max with generally high deviations. This confirms the observation made by (Zhou et al., 2016) that LSE and Max pooling strategies tend to overfit more, especially when training on few samples. From Tab.5, we can also observe that the classification performance (both in term of accuracy and AP) is the best at $200\times$ and $40\times$ magnifications. This suggests that both level of magnification are ideal for BreakHis dataset with respect to the studied methods. This is further confirmed by the accuracy obtained when training only on a fraction of the dataset Fig.17. When using 25% of the training set, the accuracy of most methods is still at around $\sim 90\%$ at magnification of $200\times$ and $40\times$ as opposed to $100\times$ and $400\times$ magnification. However, the magnification $200\times$ seems to be more stable and robust toward the variation of the number of training samples. The magnification $400\times$ shows to be the worse. These results suggest that the visual discriminative features for cancer grading using the studied approach are better observed at low magnification (zoom-out) –i.e., between $40\times$ and $200\times$ –. Zooming-in further into the histology image –e.g., $400\times$ –, makes it difficult to discriminate between the different classes. This may also suggest that when zooming-in further, this type of imaging provides almost similar images independently from the cancer grade.

We also note that Deep MIL has high variation in term of classification performance when the number of training samples is heavily reduced in the case of BreakHis dataset Fig.17 which suggests that such method needs a larger number of training sample to converge.

In the case of BACH dataset, increasing the size of the training samples leads to an improvement of in classification performance across all the methods (Fig.16) which is a typical behavior in ML algorithms.

Table 5: **Evaluation A:** Average of mean \pm standard deviation of accuracy, and AP over test folds of BreakHis (Spanhol et al., 2016b) dataset using different magnification factors and different models.

Method	Magnification		40 \times		100 \times		200 \times		400 \times	
	Method	Accuracy (%)	AP (%)							
CAM - Average		92.19 \pm 3.54	97.80 \pm 2.30	89.64 \pm 2.93	98.10 \pm 0.91	91.03 \pm 1.33	98.36 \pm 0.54	85.09 \pm 2.09	96.04 \pm 0.99	
Max		90.09 \pm 2.89	97.64 \pm 2.01	88.11 \pm 3.08	97.75 \pm 1.22	90.41 \pm 2.66	98.21 \pm 0.70	84.00 \pm 1.95	95.44 \pm 1.16	
LSE		89.52 \pm 3.68	97.04 \pm 2.96	89.57 \pm 3.24	97.92 \pm 1.00	90.15 \pm 1.96	98.08 \pm 0.79	84.86 \pm 1.98	95.16 \pm 1.74	
WILDCAT		92.40 \pm 2.82	97.90 \pm 2.41	90.22 \pm 2.48	97.99 \pm 1.55	90.75 \pm 2.00	98.49 \pm 0.59	85.85 \pm 3.05	96.41 \pm 1.40	
Deep MIL		91.80 \pm 2.70	98.38 \pm 1.64	89.54 \pm 3.14	97.69 \pm 1.16	91.61 \pm 1.34	98.71 \pm 0.55	85.98 \pm 2.28	96.29 \pm 0.85	

Table 6: **Evaluation A:** Accuracy and mAP over test folds on the BACH (Part A) dataset (Aresta et al., 2018) using different models.

Method	Accuracy (%)	mAP (%)
CAM - Average	84.10 \pm 2.51	93.23 \pm 1.27
Max	76.10 \pm 3.60	87.34 \pm 4.44
LSE	78.90 \pm 4.29	88.73 \pm 2.77
WILDCAT	84.80 \pm 1.25	93.04 \pm 1.00
Deep MIL (adapted)	83.30 \pm 3.90	92.68 \pm 2.71

Table 7: **Evaluation A and B:** Dice index, accuracy over the test folds of GlaS (Sirinukunwattana et al., 2017) dataset using different models. AP is not shown since weakly supervised localization methods always achieve 100%.

Method	Dice index	Accuracy (%)
CAM - Average	68.43 \pm 0.73	99.75 \pm 0.56
GradCAM	68.48 \pm 0.72	99.75 \pm 0.56
Max	67.51 \pm 2.48	99.75 \pm 0.56
LSE	65.61 \pm 3.73	99.50 \pm 0.68
WILDCAT	68.62 \pm 0.61	100 \pm 0
Deep MIL (adapted)	72.13 \pm 1.78	99.25 \pm 1.12
U-Net	90.54 \pm 0.88	-

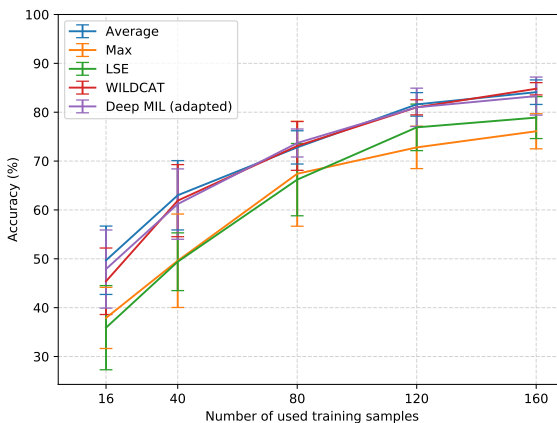


Figure 16: Influence of the training set size for the BACH dataset.

Fig.16,17 also suggest that in order to obtain a good classification accuracy of $\sim 80\%$, models require at least ~ 40 samples per class for BACH dataset, and ~ 40 samples per class for BreakHis ($\sim 10\%$).

5.2. Evaluation B – localization performance:

Tab.7 and Tab.9 correspond to the evaluation of different deep weakly supervised localization techniques over GlaS and CAMELYON16 datasets, respectively, in term of localization performance. In term of Dice index, we observe that Deep MIL obtains the best performance on GlaS dataset while Max and LSE pooling have worse results and higher variation. This suggests that both methods have a tendency to overfit more and they are more sensitive to data variations through cross-validation. For CAMELYON16 dataset, we notice that all the methods except Deep MIL achieve relatively in similar Dice index over the entire test set. Max and LSE have much lower performance on large patches. This is due to the fact that these methods tend to overfit on small discriminative regions which represent a much small fraction of the images in a large patch which results in a low Dice index. The performance in term of Dice index of Deep MIL is however not representative due the way we have adapted it. It tends to predict positive –i.e., metastatic– regions all over the images. For this reason, we also report the mean Dice index over metastatic images to measure how well it predicts positive regions. This measure shows that Deep MIL is able to correctly identify positive regions compared to other techniques.

We provide in Appendix A visual examples of the predicted masks for pixel-level localization produced by the different studied deep weakly supervised localization techniques over GlaS and CAMELYON16 test sets of the first split. From Fig.A.18, A.19, A.20, A.21 the main observation is the high false positive rate. The models are enable to correctly spot the right regions of interest, and, they tend to be active all over the image.

Table 8: **Evaluation A:** Accuracy and AP obtained with weakly supervised localization models for test folds of CAMELYON16 (Ehteshami Bejnordi et al., 2017) dataset using growing patch size.

Method	Patch size (512, 512)		Patch size (768, 768)		Patch size (1,024, 1,024)	
	Accuracy (%)	AP (%)	Accuracy (%)	AP (%)	Accuracy (%)	AP (%)
CAM - Average	98.54 \pm 0.36	99.80 \pm 0.04	98.37 \pm 0.45	99.89 \pm 0.03	99.20 \pm 0.28	99.92 \pm 0.02
Max	98.51 \pm 0.22	99.80 \pm 0.04	98.62 \pm 0.27	99.90 \pm 0.04	87.07 \pm 11.59	92.45 \pm 12.29
LSE	98.62 \pm 0.22	99.80 \pm 0.04	98.77 \pm 0.22	99.92 \pm 0.02	93.41 \pm 0.67	98.44 \pm 0.27
WILDCAT	98.37 \pm 0.65	99.84 \pm 0.05	98.62 \pm 0.36	99.92 \pm 0.03	99.16 \pm 0.17	99.95 \pm 0.01
Deep MIL	98.15 \pm 0.59	99.82 \pm 0.04	98.34 \pm 1.16	99.82 \pm 0.23	99.17 \pm 0.11	99.95 \pm 0.01

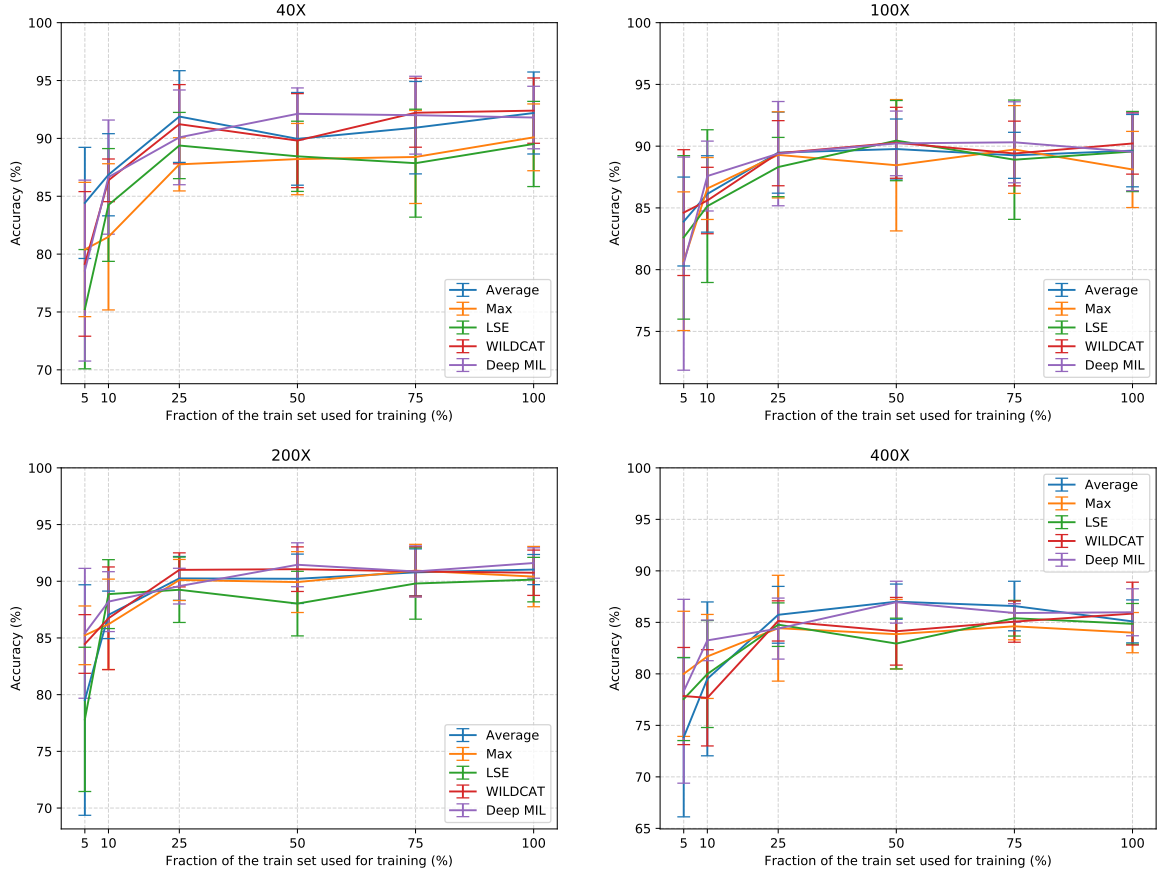


Figure 17: Influence of the training set size for the BreakHis dataset at magnification levels of 40 \times (top left), 100 \times (top right), 200 \times (bottom left) and 400 \times (bottom right).

Table 9: **Evaluation B**: Dice index over all pixels and averaged over all metastatic images (mDice metastatic) obtained with weakly supervised localization models for test folds of CAMELYON16 (Ehteshami Bejnordi et al., 2017) dataset using a growing patch size.

Method	(512, 512)		(768, 768)		(1,024, 1,024)	
	Dice index	mDice metastatic	Dice index	mDice metastatic	Dice index	mDice metastatic
CAM - Average	65.06 \pm 1.00	62.47 \pm 1.17	64.16 \pm 0.78	61.45 \pm 0.67	66.70 \pm 2.77	63.98 \pm 2.93
GradCAM	65.18 \pm 1.02	62.51 \pm 1.19	64.14 \pm 0.86	61.35 \pm 0.75	66.75 \pm 2.76	63.98 \pm 2.95
Max	67.08 \pm 1.33	62.31 \pm 1.10	68.50 \pm 1.43	63.51 \pm 1.02	50.23 \pm 12.45	55.71 \pm 5.73
LSE	67.04 \pm 1.30	62.78 \pm 0.87	64.96 \pm 3.96	61.71 \pm 1.81	62.97 \pm 7.34	60.19 \pm 8.15
WILDCAT	66.06 \pm 0.84	62.87 \pm 0.86	67.24 \pm 1.29	63.74 \pm 1.33	66.05 \pm 2.96	65.52 \pm 1.28
Deep MIL	49.26 \pm 2.81	69.76 \pm 0.73	47.93 \pm 2.66	68.49 \pm 2.16	46.61 \pm 2.81	65.97 \pm 1.67
U-Net	77.68 \pm 1.47	70.90 \pm 2.37	79.90 \pm 1.30	73.03 \pm 2.05	80.72 \pm 0.83	72.79 \pm 1.47

The studied deep weakly supervised localization have been developed, validated, and improved over the years mainly over natural scene images which reinforce many implicit priors of such type of images in their conception. We believe that applying them directly to histology images for weakly supervised localization tasks can lead to poor and unexpected results in term of localization of regions of interest as illustrated visually in Fig.A.18, A.19, A.20, A.21. This behavior is mainly a direct result of the nature of histology images where objects of interest are highly unstructured, variable in size, multi-instance presence, and more importantly, non-salient. Often, in a histology image, regions of interest have similar visual appearance in term of texture/color with respect to the background. This may potentially mislead the models and result in a high false positive rate. Therefore, applying the studied weakly supervised localization techniques in histology may require an adaptation to improve the selectivity of regions of interest and reduce false positive rate. A promising approach has been proposed recently where modeling irrelevant region within the image is taken in consideration which allows to reduce false positive with a large gap (Belharbi et al., 2019). High false positive rate damages the interpretability aspect of weakly supervised localization techniques, and lower their usefulness in a weak localization task in histology images.

Another explanation to the high false positive rate is related to the pooling function. All the evaluated methods need to perform a spatial pooling to be able to classify the input image. A model is trained to predict either benign or malignant cancer grade by maximizing the probability of the target class. For a method such as CAM with Average pooling, this will attempt to maximize the probability of the target class by maximizing scores over every location in the

image in order to maximize the global probability for that class since all locations in histology images are practically similar in term of visual perception. Adding to this the issue of noisy labels of patches during training discussed in Sec.2.3. As a result, this allows to consider non-discriminative regions as discriminative –i.e., consider noise/background as regions of interest–. Therefore, high false positive rate is increased. This problem may be addressed by adding more supervision (Jia et al., 2017) in the form on size constraints. However, this will face the challenge of the high variation of the size of object of interest in histology images that goes from tiny regions to almost cover an entire image. Adding noise –i.e., uncertainty– to the target label at patch level may help reducing the issue of the inconsistency that may raise when transferring the image label to the patch label (Szegedy et al., 2016).

It is also interesting to note that the U-Net trained in a fully supervised fashion does perform significantly better than weakly supervised models for smaller patches. This may come from the architecture. ResNet architecture may be better suited to correctly classify images while U-Net can have a better coherence in the local prediction (higher Dice index over all images). It might be interesting to evaluate more recent state-of-the-art segmentation architectures such as DeepLabV3+ (Chen et al., 2018) and HRNet (Sun et al., 2019) to get a stronger fully supervised baseline, as these architectures combine the benefits of both ResNet-like architecture and segmentation-specific architectural improvements.

5.3. Future directions:

Upon our empirical evaluation and the obtain results, the application of computer vision deep weakly supervised localization techniques over histology images showed that in term of classification, these

techniques still achieve high performance. However, in term of localization of regions of interest, they are still behind and results in a high false positive rate mainly due to the nature of histology images that is different from the one of natural scene images. Such poor localization can downgrade the interpretability value in such deep weakly supervised localization techniques in this medical application.

While using full pixel-level supervision for object localization in histology images has a high cost in term of labeling, our results suggest that the other extreme case –i.e., learning to localize without pixel-level labels– can result in poor localization. As a potential compromise and a future direction, few-shot learning (Rakelly et al., 2018; Wang and Yao, 2019) where only very few samples are labeled at pixel-level can be a promising research direction in our application. From one hand, the pathologist needs to label only few samples at pixel-level. Such scarce but extremely valuable annotation will hopefully provide a strong hint about the nature of regions of interest during learning, which, in turn, will potentially reduce the false positive rate of localization. While such direction relies on a fixed number of pre-annotated samples, another research direction may consider a dynamically increasing number of annotated samples upon request. This can be very helpful to deal with high resolution images. In such scenario, the model requests the pathologist to annotate at pixel-level the most relevant region at a training step. This prevents annotating irrelevant regions and save the pathologist’s time. Active learning methods (Settles, 2009) allow such learning scheme which we consider as a second research direction for regions of interest localization in histology images with low cost in term of pixel-level annotation.

A minor but important point that is worth mentioning is related to cancer grading and its impact on the image label and regions of interest localization. As mentioned in the key challenges of histology images, many grades may be present in the image, where only the worse is provided as image label. Therefore, in order to localize regions of interest, the learning process may also consider such multi-grades presence by using multi-label learning scenario instead of considering one single hard label in the image. Using this prior of simultaneous presence of grades may help improving the precision of regions localization and reduce false positive, since it will boost the awareness of the model and prevent it from associating the entire image into one single

label.

6. Conclusion

We have presented in this paper a survey on state-of-the-art deep weakly supervised localization methods which have been developed in computer vision community mostly for natural scene images, and evaluated their application on histology image analysis for cancer identification and localization. Such methods are able to classify an image and spot regions of interest within an image, simultaneously. We presented the process of histology image production, and identified their main key challenges including their large size, non-salient/highly unstructured regions, stain heterogeneity, and coarse/ambiguous labels. The high resolution of these images makes their annotation at pixel-level a tedious, and time consuming task which places a burden on building large corpora of histology images in order train ML methods. Motivated by this issue, we have explored the application of these deep weakly supervised localization techniques in histology images in order to localize regions of interest at pixel-level *without* pixel-level supervision.

Upon our taxonomization of different state-of-the-art deep weakly supervised localization techniques, we have selected a set of techniques for our evaluation (CAM, WILDCAT, and Deep MIL from bottom-up methods; and Grad-CAM method from top-down category.). In our experiments, our main interest was to evaluate the selected methods, which are trained only using global image label and deprived from pixel-level supervision, in terms of (1) image classification and (2) pixel-level localization of regions of interest. To this end, a benchmark of different public histological datasets for breast and colon cancer: BreakHis, BACH, GlaS, and CAMELYON16 was used. In the literature, public histological datasets with *both* image-level and pixel-level annotation are extremely rare. Many interesting benchmarks are private, unfortunately. In this survey, GlaS dataset is the only one that fills such criterion. In order to provide more histology image benchmarks, and perform large scale evaluations, we proposed a concise protocol to build WSL datasets from Whole Slide Images (WSI). This protocol was used to create new weakly supervised localization benchmark from CAMELYON16. Cross-validation with a fixed test set was considered to measure the robustness of the different methods on both tasks. For the evaluation metrics, we used standard

accuracy for classification performance, and Dice index for pixel-level localization performance. The deterministic code used for splitting the datasets for cross-validation, sampling from CAMELYON16 dataset, coordinates of the samples, and the code of the experiments is made public¹⁶.

In term of classification performance, the experimental evaluation of the selected methods showed a high accuracy across all the datasets with slight difference between the methods. BACH dataset seems to be more challenging. Overall, WILDCAT and deep MIL methods showed to be the best methods at this task.

In term of pixel-level localization, the results showed a high false positive rate indicating that such methods are unable to correctly localize relevant regions which are confused with the background. Compared to full supervision results, weak localization results are still way behind. These results raise the question of the usefulness of the studied weakly supervised localization methods in our application. Such techniques have been developed, validated, and improved over the years on natural scene images which reinforced many priors of this type of images in their conception. Therefore, applying them in histology images may require an adaptation to improve their selectivity of regions of interest and reduce false positive rate. A promising approach has been proposed recently where modeling irrelevant regions within the image was taken in consideration which allowed to reduce false positive rate with a large gap (Belharbi et al., 2019). Few-shot learning and active learning can be considered as well as an alternative and future research directions that allow cancer grading and localization in histology images with low cost for pixel-level annotation.

References

Aresta, G., Araujo, T., Kwok, S., et al., 2018. Bach: Grand challenge on breast cancer histology images. *coRR* abs/1808.04277.

Bahdanau, D., Cho, K., Bengio, Y., 2014. Neural machine translation by jointly learning to align and translate. *CoRR* abs/1409.0473.

Bamford, P., Lovell, B., 2001. Method for accurate unsupervised cell nucleus segmentation, in: *Conf. of the Intern. Conf. of the IEEE Engineering in Medicine and Biology Society*.

Bankman, I., 2008. *Handbook of medical image processing and analysis*. Elsevier.

Bartels, P., Thompson, D., Bibbo, M., et al., 1992. Bayesian belief networks in quantitative histopathology. *Analytical and quantitative cytology and histology* 14.

Basavanhally, A., Agner, S., Alexe, G., et al., 2008. Manifold learning with graph-based features for identifying extent of lymphocytic infiltration from high grade, her2+ breast cancer histology.

Belharbi, S., Rony, J., Dolz, J., Ben Ayed, I., McCaffrey, L., Granger, E., 2019. Weakly supervised object localization using min-max entropy: an interpretable framework. *coRR* abs/1907.12934.

Bency, A.J., Kwon, H., Lee, H., et al., 2016. Weakly supervised localization using deep feature maps, in: *ECCV*.

Bilen, H., Pedersoli, M., Tuytelaars, T., 2014. Weakly supervised object detection with posterior regularization, in: *BMVC*.

Bilen, H., Pedersoli, M., Tuytelaars, T., 2015. Weakly supervised object detection with convex clustering, in: *CVPR*.

Bilen, H., Vedaldi, A., 2016. Weakly supervised deep detection networks, in: *CVPR*.

Bilgin, C., Demir, C., Nagi, C., et al., 2007. Cell-graph mining for breast tissue modeling and classification, in: *Intern. Conf. of the IEEE Engineering in Medicine and Biology Society*.

Boyd, S., Vandenberghe, L., 2004. *Convex Optimization*. Cambridge University Press.

Bándi, P., Geessink, O., Manson, Q., et al., 2019. From detection of individual metastases to classification of lymph node status at the patient level: The camelyon17 challenge. *IEEE Transactions on Medical Imaging* 38.

Caicedo, J.C., González, F.A., Romero, E., 2011. Content-based histopathology image retrieval using a kernel-based semantic annotation framework. *Jour. of biomedical informatics* 44.

Caie, P.D., Turnbull, A.K., Farrington, S.M., et al., 2014. Quantification of tumour budding, lymphatic vessel density and invasion through image analysis in colorectal cancer. *Journal of translational medicine* 12.

Cao, C., Liu, X., Yang, Y., et al., 2015. Look and think twice: Capturing top-down visual attention with feedback convolutional neural networks, in: *ICCV*.

Carboneau, M.A., Cheplygina, V., Granger, E., Gagnon, G., 2018. Multiple instance learning: A survey of problem characteristics and applications. *Pattern Recognition* 77, 329–353.

Chandler, D.E., Roberson, R.W., 2009. *Bioimaging: current concepts in light and electron microscopy*. Jones & Bartlett Publishers.

Chattopadhyay, A., Sarkar, A., Howlader, P., et al., 2018. Grad-cam++: Generalized gradient-based visual explanations for deep convolutional networks, in: *WACV*.

Chen, H., Qi, X., Yu, L., et al., 2016. Dcan: deep contour-aware networks for accurate gland segmentation, in: *CVPR*.

Chen, L.C., Zhu, Y., Papandreou, G., Schroff, F., Adam, H., 2018. Encoder-decoder with atrous separable convolution for semantic image segmentation, in: *ECCV*.

Cheplygina, V., de Bruijne, M., Pluim, J., 2019. Not-so-supervised: A survey of semi-supervised, multi-instance, and transfer learning in medical image analysis. *MIA* 54.

Cinbis, R.G., Verbeek, J., Schmid, C., 2017. Weakly supervised object localization with multi-fold multiple instance learning. *IEEE trans. on pattern analysis and machine intelligence* 39.

Ciompi, F., Geessink, O., Bejnordi, B.E., et al., 2017. The

¹⁶https://github.com/jeromerony/survey_wsl_histology

importance of stain normalization in colorectal tissue classification with convolutional networks, in: Biomedical Imaging.

Cireşan, D.C., Giusti, A., Gambardella, L.M., et al., 2013. Mitosis detection in breast cancer histology images with deep neural networks, in: MICCAI.

Cooper, L., Sertel, O., Kong, J., et al., 2009. Feature-based registration of histopathology images with different stains: An application for computerized follicular lymphoma prognosis. Computer methods and programs in biomedicine 96.

Courtial, P., Tramel, E.W., Sanselme, M., et al., 2018. Classification and disease localization in histopathology using only global labels: A weakly-supervised approach. coRR abs/1802.02212.

Couture, H.D., Marron, J., Perou, C.M., et al., 2018. Multiple instance learning for heterogeneous images: Training a cnn for histopathology. coRR abs/1806.05083.

Daisuke, K., Shumpei, I., 2018. Machine learning methods for histopathological image analysis. Computational and Structural Biotechnology Journal 16.

Deng, J., Dong, W., Socher, R., et al., 2009. Imagenet: A large-scale hierarchical image database, in: CVPR.

Diba, A., Sharma, V., Pazandeh, A.M., et al., 2017. Weakly supervised cascaded convolutional networks, in: CVPR.

Dice, L.R., 1945. Measures of the amount of ecological association between species. Ecology 26.

Dolz, J., Desrosiers, C., Ben Ayed, I., 2018. 3D fully convolutional networks for subcortical segmentation in MRI: A large-scale study. NeuroImage .

Doshi-Velez, F., Kim, B., 2017. Towards a rigorous science of interpretable machine learning. coRR abs/1702.08608.

Doyle, S., Agner, S., Madabhushi, A., et al., 2008. Automated grading of breast cancer histopathology using spectral clustering with textural and architectural image features, in: Intern. Symposium on Biomedical Imaging: From Nano to Macro.

Doyle, S., Hwang, M., Shah, K., et al., 2007. Automated grading of prostate cancer using architectural and textural image features, in: Intern. Symposium on Biomedical Imaging: From Nano to Macro.

Doyle, S., Madabhushi, A., Feldman, M., et al., 2006a. A boosting cascade for automated detection of prostate cancer from digitized histology, in: MICCAI.

Doyle, S., Rodriguez, C., Madabhushi, A., et al., 2006b. Detecting prostatic adenocarcinoma from digitized histology using a multi-scale hierarchical classification approach, in: Intern. Conf. of the IEEE Engineering in Medicine and Biology Society.

Durand, T., Mordan, T., Thome, N., et al., 2017. Wildcat: Weakly supervised learning of deep convnets for image classification, pointwise localization and segmentation, in: CVPR.

Durand, T., Thome, N., Cord, M., 2015. MANTRA: Minimum Maximum Latent Structural SVM for Image Classification and Ranking, in: ICCV.

Durand, T., Thome, N., Cord, M., 2016. Weldon: Weakly supervised learning of deep convolutional neural networks, in: CVPR.

Ehteshami Bejnordi, B., Veta, M., Johannes van Diest, P., et al., 2017. Diagnostic Assessment of Deep Learning Algorithms for Detection of Lymph Node Metastases in Women With Breast CancerMachine Learning Detection of Breast Cancer Lymph Node MetastasesMachine Learning Detection of Breast Cancer Lymph Node Metastases.

JAMA 318.

Everingham, M., Van Gool, L., Williams, C.K.I., et al., 2010. The pascal visual object classes (voc) challenge. IJCV 88.

Feng, X., Yang, J., Laine, A.F., et al., 2017. Discriminative localization in cnns for weakly-supervised segmentation of pulmonary nodules, in: MICCAI.

Frenay, B., Verleysen, M., 2014. Classification in the presence of label noise: A survey. TNNLS 25.

Gartner, L.P., Hiatt, J.L., 2006. Color textbook of histology: with student consult online access.

Ge, W., Yang, S., Yu, Y., 2018. Multi-evidence filtering and fusion for multi-label classification, object detection and semantic segmentation based on weakly supervised learning, in: CVPR.

Gertych, A., Ing, N., Ma, Z., et al., 2015. Machine learning approaches to analyze histological images of tissues from radical prostatectomies. Computerized Medical Imaging and Graphics 46.

Girshick, R., 2015. Fast r-cnn, in: ICCV.

Gondal, W.M., Köhler, J.M., Grzeszick, R., et al., 2017. Weakly-supervised localization of diabetic retinopathy lesions in retinal fundus images, in: ICIP.

Goodfellow, I., Bengio, Y., Courville, A., 2016. Deep Learning. MIT Press. <http://www.deeplearningbook.org>.

Greenberg, S.D., 1984. Computer-assisted image analysis cytology. Karger, S Publishers.

Guillaud, M., Adler-Storthz, K., Malpica, A., et al., 2005. Subvisual chromatin changes in cervical epithelium measured by texture image analysis and correlated with hpv. Gynecologic oncology 99.

Guillaud, M., Cox, D., Malpica, A., et al., 2004. Quantitative histopathological analysis of cervical intra-epithelial neoplasia sections: methodological issues 26.

Gurcan, M., Pan, T., Shimada, H., et al., 2006. Image analysis for neuroblastoma classification: Hysteresis thresholding for cell segmentation.

Gurcan, M.N., Boucheron, L., Can, A., et al., 2009. Histopathological image analysis: A review. IEEE reviews in biomedical engineering 2.

Hamilton, P., Anderson, N., Bartels, P., et al., 1994. Expert system support using bayesian belief networks in the diagnosis of fine needle aspiration biopsy specimens of the breast. Journal of clinical pathology 47.

He, K., Zhang, X., Ren, S., et al., 2014. Spatial pyramid pooling in deep convolutional networks for visual recognition, in: ECCV.

He, K., Zhang, X., Ren, S., et al., 2016. Deep residual learning for image recognition, in: CVPR.

He, L., 2009. Towards image understanding: deformable contour and graph-based image segmentation and recognition. Lambert Academic Publishing.

He, L., Long, L.R., Antani, S., et al., 2010. Computer assisted diagnosis in histopathology. Sequence and genome analysis: methods and applications 15.

He, L., Long, L.R., Antani, S., et al., 2012. Histology image analysis for carcinoma detection and grading. Computer methods and programs in biomedicine 107.

Hipp, J.D., Fernandez, A., Compton, C.C., et al., 2011. Why a pathology image should not be considered as a radiology image. Journal of pathology informatics 2.

Hou, L., Samaras, D., Kurc, T.M., et al., 2016. Patch-based convolutional neural network for whole slide tissue image classification, in: CVPR.

Ise, M., Tomczak, J.M., Welling, M., 2018. Attention-based deep multiple instance learning. coRR abs/1802.04712.

Izadyyyazdanabadi, M., Belykh, E., Cavallo, C., et al., 2018. Weakly-supervised learning-based feature localization in confocal laser endomicroscopy glioma images. *coRR* abs/1804.09428.

Janowczyk, A., Basavanhally, A., Madabhushi, A., 2017. Stain normalization using sparse autoencoders (stanosa): Application to digital pathology. *Computerized Medical Imaging and Graphics* 57.

Janowczyk, A., Madabhushi, A., 2016. Deep learning for digital pathology image analysis: A comprehensive tutorial with selected use cases. *Jour. of pathology informatics* 7.

Jia, Z., Huang, X., Eric, I., Chang, C., Xu, Y., 2017. Constrained deep weak supervision for histopathology image segmentation. *IEEE transactions on medical imaging* 36, 2376–2388.

Jie, Z., Wei, Y., Jin, X., et al., 2017. Deep self-taught learning for weakly supervised object localization, in: *CVPR*.

Jütting, U., Gais, P., Rodenacker, K., et al., 1999. Diagnosis and prognosis of neuroendocrine tumours of the lung by means of high resolution image analysis. *Analytical Cellular Pathology* 18.

Kandemir, M., Hamprecht, F., 2015. Computer-aided diagnosis from weak supervision: A benchmarking study. *Computerized medical imaging and graphics* 42.

Kantorov, V., Oquab, M., Cho, M., et al., 2016. Context-locnet: Context-aware deep network models for weakly supervised localization, in: *ECCV*.

Kayser, G., Riede, U., Werner, M., et al., 2002. Towards an automated morphological classification of histological images of common lung carcinomas. *Elec J Pathol Histol* 8.

Kieffer, B., Babaie, M., Kalra, S., et al., 2017. Convolutional neural networks for histopathology image classification: Training vs. using pre-trained networks, in: *Intern. Conf. on Image Processing Theory, Tools and Applications*.

Kiernan, J.A., 1990. Histological and histochemical methods: theory and practice. volume 20. Pergamon press Oxford.

Kong, J., Sertel, O., Lozanski, G., et al., 2007a. Automated detection of follicular centers for follicular lymphoma grading, in: *Advancing Practice, Instruction, and Innovation Through Informatics Conf.*

Kong, J., Shimada, H., Boyer, K., et al., 2007b. Image analysis for automated assessment of grade of neuroblastic differentiation, in: *Intern. Symposium on Biomedical Imaging: From Nano to Macro*.

Krizhevsky, A., Sutskever, I., Hinton, G.E., 2012. Imagenet classification with deep convolutional neural networks, in: *NIPS*.

Lamprecht, M.R., Sabatini, D.M., Carpenter, A.E., 2007. CellprofilerTM: free, versatile software for automated biological image analysis. *Biotechniques* 42.

Li, Y., Ping, W., 2018. Cancer metastasis detection with neural conditional random field, in: *Medical Imaging with Deep Learning*.

Lin, M., Chen, Q., Yan, S., 2013. Network in network. *coRR* abs/1312.4400.

Lin, T.Y., Maire, M., Belongie, S., et al., 2014. Microsoft coco: Common objects in context, in: *ECCV*.

Lipton, Z.C., 2018. The mythos of model interpretability. *Queue* 16.

Litjens, G., Kooi, T., Bejnordi, B.E., et al., 2017. A survey on deep learning in medical image analysis. *MIA* .

Liu, W., Anguelov, D., Erhan, D., et al., 2016. Ssd: Single shot multibox detector, in: *ECCV*.

Madabhushi, A., 2009. Digital pathology image analysis: opportunities and challenges. *Imaging in medicine* 1.

Marcus, G., 2001. *The algebraic mind: Integrating connectionism and cognitive science*. MIT Press.

Marcus, G., 2018. Deep learning: A critical appraisal. *CoRR* abs/1801.00631.

Méndez, A.J., Tahoces, P.G., Lado, M.J., et al., 1998. Computer-aided diagnosis: Automatic detection of malignant masses in digitized mammograms. *Medical Physics* 25.

Mescher, A.L., 2013. Junqueira's basic histology: text and atlas. volume 12. McGraw-Hill Medical.

Molnar, C., et al., 2018. Interpretable machine learning: A guide for making black box models explainable.

Mungle, T., Tewary, S., Das, D., et al., 2017. Mrf-ann: a machine learning approach for automated er scoring of breast cancer immunohistochemical images. *Journal of microscopy* 267.

Murphy, D.B., Davidson, M.W., 2001. *Fundamentals of light microscopy and electronic imaging*. volume 184. Wiley Online Library.

Naik, S., Doyle, S., Madabhushi, A., et al., 2007. Automated gland segmentation and gleason grading of prostate histology by integrating low-, high-level and domain specific information, in: *Workshop on Microscopic Image Analysis with Applications in Biology*.

Nelson, D.L., Lehninger, A.L., Cox, M.M., 2008. *Lehninger principles of biochemistry*. Macmillan.

O'Neil, C., 2016. *Weapons of Math Destruction: How Big Data Increases Inequality and Threatens Democracy*. Crown Publishing Group.

Oquab, M., Bottou, L., Laptev, I., et al., 2015. Is object localization for free?-weakly-supervised learning with convolutional neural networks, in: *CVPR*.

Otsu, N., 1979. A threshold selection method from gray-level histograms. *IEEE Trans. on Systems, Man, and Cybernetics* 9.

Petushi, S., Garcia, F.U., Haber, M.M., et al., 2006. Large-scale computations on histology images reveal grade-differentiating parameters for breast cancer. *BMC medical imaging* 6.

Pinheiro, P.H.O., Collobert, R., 2015a. From image-level to pixel-level labeling with convolutional networks, in: *CVPR*.

Pinheiro, P.O., Collobert, R., 2015b. From image-level to pixel-level labeling with convolutional networks, in: *CVPR*.

Quellec, G., Cazuguel, G., Cochener, B., Lamard, M., 2017. Multiple-instance learning for medical image and video analysis. *IEEE reviews in biomedical engineering* 10.

Qureshi, H., Sertel, O., Rajpoot, N., et al., 2008. Adaptive discriminant wavelet packet transform and local binary patterns for meningioma subtype classification, in: *MICCAI*.

Rakelly, K., Shelhamer, E., Darrell, T., et al., 2018. Few-shot segmentation propagation with guided networks. *CoRR* abs/1806.07373.

Redmon, J., Divvala, S.K., Girshick, R.B., et al., 2016. You only look once: Unified, real-time object detection, in: *CVPR*.

Ribeiro, M.T., Singh, S., Guestrin, C., 2016. "why should i trust you?": Explaining the predictions of any classifier, in: *ACM SIGKDD 2016*.

Ronneberger, O., Fischer, P., Brox, T., 2015. U-net: Convolutional networks for biomedical image segmentation, in: *MICCAI*.

Ross, M., Kaye, G., Pawlina, W., 2003. Histology a text and atlas.

Roux, L., Racoceanu, D., Loménie, N., et al., 2013. Mitosis detection in breast cancer histological images an icpr 2012 contest. *Jour. of pathology informatics* 4.

Samek, W., Wiegand, T., Müller, K.R., 2017. Explainable artificial intelligence: Understanding, visualizing and interpreting deep learning models. *coRR* abs/1708.08296.

Van de Sande, K.E., Uijlings, J.R., Gevers, T., et al., 2011. Segmentation as selective search for object recognition, in: *ICCV*.

Schroeder, W., Ng, L., Cates, J., 2003. The itk software guide.

Sedai, S., Mahapatra, D., Ge, Z., et al., 2018. Deep multi-scale convolutional feature learning for weakly supervised localization of chest pathologies in x-ray images, in: *Intern. Workshop on Machine Learning in Medical Imaging*.

Selvaraju, R.R., Cogswell, M., Das, A., et al., 2017. Grad-cam: Visual explanations from deep networks via gradient-based localization, in: *ICCV*.

Settles, B., 2009. Active learning literature survey. Technical Report. University of Wisconsin-Madison Department of Computer Sciences.

Shah, M., Wang, D., Rubadue, C., et al., 2017. Deep learning assessment of tumor proliferation in breast cancer histological images, in: *Intern. Conf. on Bioinformatics and Biomedicine*.

Sheikhzadeh, F., Guillaud, M., Ward, R.K., 2016. Automatic labeling of molecular biomarkers of whole slide immunohistochemistry images using fully convolutional networks. *coRR* abs/1612.09420.

Shen, Y., Ji, R., Zhang, S., et al., 2018. Generative adversarial learning towards fast weakly supervised detection, in: *CVPR*.

Shimodaira, H., 2000. Improving predictive inference under covariate shift by weighting the log-likelihood function. *Journal of statistical planning and inference* 90.

Sirinukunwattana, K., Pluim, J.P., Chen, H., et al., 2017. Gland segmentation in colon histology images: The glas challenge contest. *MIA* 35.

Spanhol, F.A., Oliveira, L.S., Petitjean, C., et al., 2016a. Breast cancer histopathological image classification using convolutional neural networks, in: *IJCNN*.

Spanhol, F.A., Oliveira, L.S., Petitjean, C., et al., 2016b. A dataset for breast cancer histopathological image classification. *IEEE Trans. on Biomedical Engineering* 63.

Sternberg, S., 1997. Histology for pathologists. volume 757. Lippincott-Raven Philadelphia.

Su, W., Yuan, Y., Zhu, M., 2015. A relationship between the average precision and the area under the roc curve, in: *Int. Conf. on The Theory of Information Retrieval*.

Sudharshan, P., Petitjean, C., Spanhol, F., et al., 2019. Multiple instance learning for histopathological breast cancer image classification. *Expert Systems with Applications* 117.

Sugiyama, M., Kawanabe, M., 2012. Machine learning in non-stationary environments: Introduction to covariate shift adaptation. MIT press.

Sukhbaatar, S., Bruna, J., Paluri, M., et al., 2014. Training convolutional networks with noisy labels. *coRR* abs/1406.2080.

Sun, C., Paluri, M., Collobert, R., et al., 2016. Pronet: Learning to propose object-specific boxes for cascaded neural networks, in: *CVPR*.

Sun, K., Zhao, Y., Jiang, B., Cheng, T., Xiao, B., Liu, D., Mu, Y., Wang, X., Liu, W., Wang, J., 2019. High-resolution representations for labeling pixels and regions. *CoRR* abs/1904.04514.

Szegedy, C., Vanhoucke, V., Ioffe, S., et al., 2016. Rethinking the inception architecture for computer vision, in: *CVPR*.

Szegedy, C., Zaremba, W., Sutskever, I., et al., 2013. Intriguing properties of neural networks. *coRR* abs/1312.6199.

Tabesh, A., Teverovskiy, M., Pang, H.Y., et al., 2007. Multi-feature prostate cancer diagnosis and gleason grading of histological images. *IEEE trans. on medical imaging* 26.

Tang, J., Rangayyan, R.M., Xu, J., et al., 2009. Computer-aided detection and diagnosis of breast cancer with mammography: recent advances. *IEEE Trans. on Information Technology in Biomedicine* 13.

Tang, P., Wang, X., Bai, X., et al., 2017. Multiple instance detection network with online instance classifier refinement, in: *CVPR*.

Tang, P., Wang, X., Wang, A., et al., 2018. Weakly supervised region proposal network and object detection, in: *ECCV*.

Teh, E.W., Rochan, M., Wang, Y., 2016. Attention networks for weakly supervised object localization, in: *BMVC*.

Török, P., Kao, F., 2007. Optical imaging and microscopy: techniques and advanced systems. volume 87. Springer.

Uijlings, J.R., Van De Sande, K.E., Gevers, T., et al., 2013. Selective search for object recognition. *IJCV* 104.

Veta, M., Heng, Y.J., Stathonikos, N., et al., 2018. Predicting breast tumor proliferation from whole-slide images: the tupac16 challenge. *coRR* abs/1807.08284.

Veta, M., Pluim, J., Van Diest, P.J., et al., 2014. Breast cancer histopathology image analysis: A review. *IEEE Transactions on Biomedical Engineering* 61.

Wan, F., Wei, P., Jiao, J., et al., 2018. Min-entropy latent model for weakly supervised object detection, in: *CVPR*.

Wang, C., Ren, W., Huang, K., et al., 2014. Weakly supervised object localization with latent category learning, in: *ECCV*.

Wang, D., Foran, D.J., Ren, J., et al., 2015. Exploring automatic prostate histopathology image gleason grading via local structure modeling, in: *Intern. Conf. the IEEE Engineering in Medicine and Biology Society*.

Wang, X., Yan, Y., Tang, P., Bai, X., Liu, W., 2018. Revisiting multiple instance neural networks. *Pattern Recognition* 74.

Wang, Y., Yao, Q., 2019. Few-shot learning: A survey. *CoRR* abs/1904.05046.

Weind, K.L., Maier, C.F., Rutt, B.K., et al., 1998. Invasive carcinomas and fibroadenomas of the breast: comparison of microvessel distributions—implications for imaging modalities. *Radiology* 208.

Wootton, R., Springall, D., Polak, J.M., et al., 1995. Image analysis in histology. CUP Archive.

Xie, J., Liu, R., Joseph Luttrell, I., et al., 2019. Deep learning based analysis of histopathological images of breast cancer. *Frontiers in genetics* .

Xu, J., Luo, X., Wang, G., et al., 2016. A deep convolutional neural network for segmenting and classifying epithelial and stromal regions in histopathological images. *Neurocomputing* 191.

Yoo, T.S., 2004. Insight into images: principles and practice for segmentation, registration, and image analysis. AK Peters/CRC Press.

Zhang, C., Bengio, S., Hardt, M., et al., 2017. Understanding deep learning requires rethinking generalization. *CoRR* abs/1611.03530.

Zhang, J., Bargal, S.A., Lin, Z., et al., 2018a. Top-down

neural attention by excitation backprop. IJCV 126.

Zhang, Q.C., Zhu, S.C., 2018. Visual interpretability for deep learning: a survey. *Frontiers of Information Technology & Electronic Engineering* 19, 27–39.

Zhang, X., Wei, Y., Feng, J., et al., 2018b. Adversarial complementary learning for weakly supervised object localization, in: CVPR.

Zhou, B., Khosla, A., Lapedriza, A., et al., 2016. Learning deep features for discriminative localization, in: CVPR.

Zhou, Z.H., 2004. Multi-instance learning: A survey. Department of Computer Science & Technology, Nanjing University, Tech. Rep .

Zhou, Z.H., 2017. A brief introduction to weakly supervised learning. NSR .

Zhu, Y., Zhou, Y., Ye, Q., et al., 2017. Soft proposal networks for weakly supervised object localization, in: ICCV.

Zitnick, C.L., Dollár, P., 2014. Edge boxes: Locating object proposals from edges, in: ECCV.

Appendix A. Visual results of pixel-level localization of regions of interest

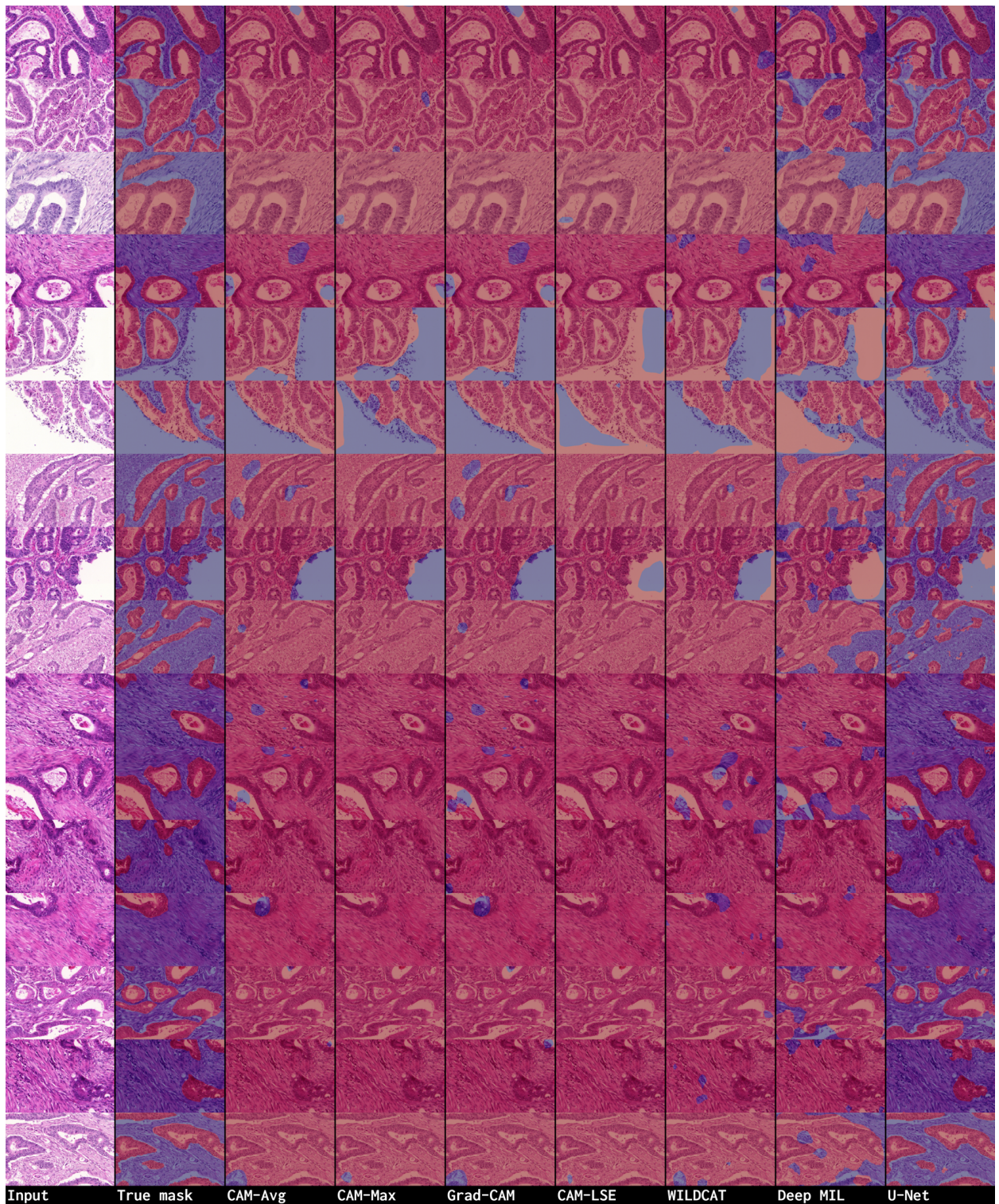


Figure A.18: Examples of visual comparison of the predicted binary mask of each WSOL method over GlaS test set (first split for the malignant class. (Best visualized in color.)

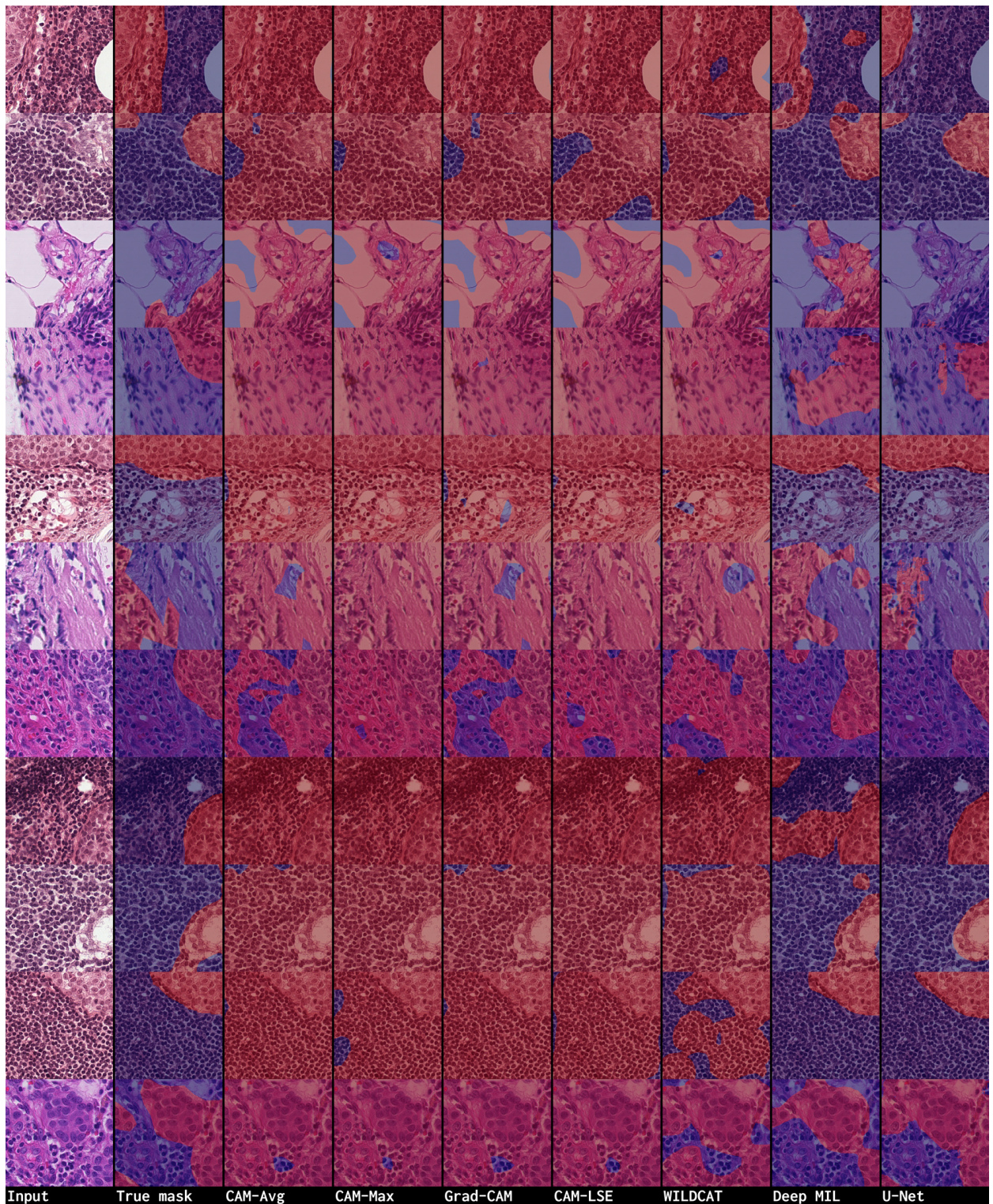


Figure A.19: Examples of visual comparison of the predicted binary mask of each WSOL method over CAMELYON16 test set (first split) for the metastatic class (patch size (512, 512)). (Best visualized in color.)

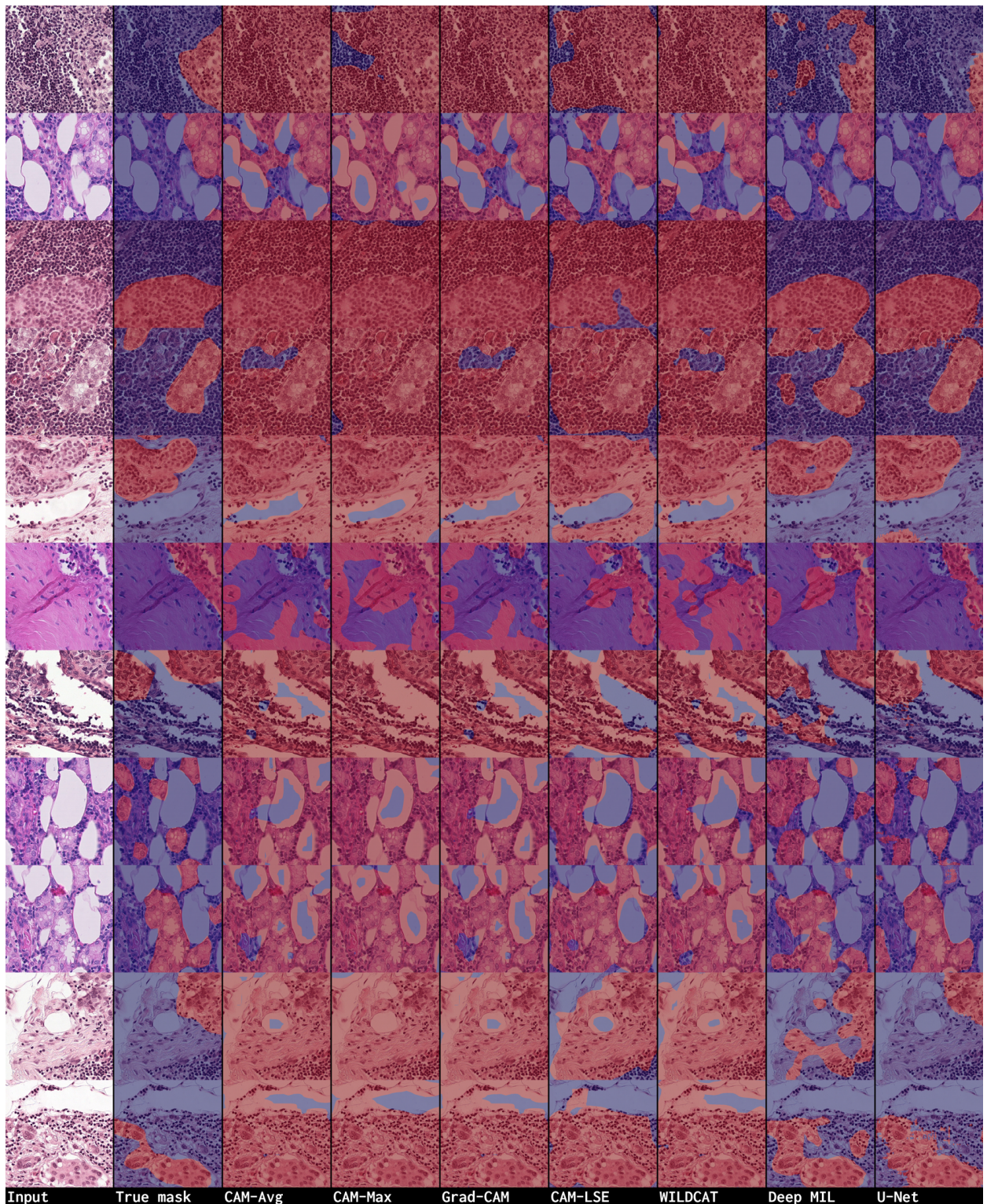


Figure A.20: Examples of visual comparison of the predicted binary mask of each WSOL method over CAMELYON16 test set (first split) for the metastatic class (patch size (768, 768)). (Best visualized in color.)

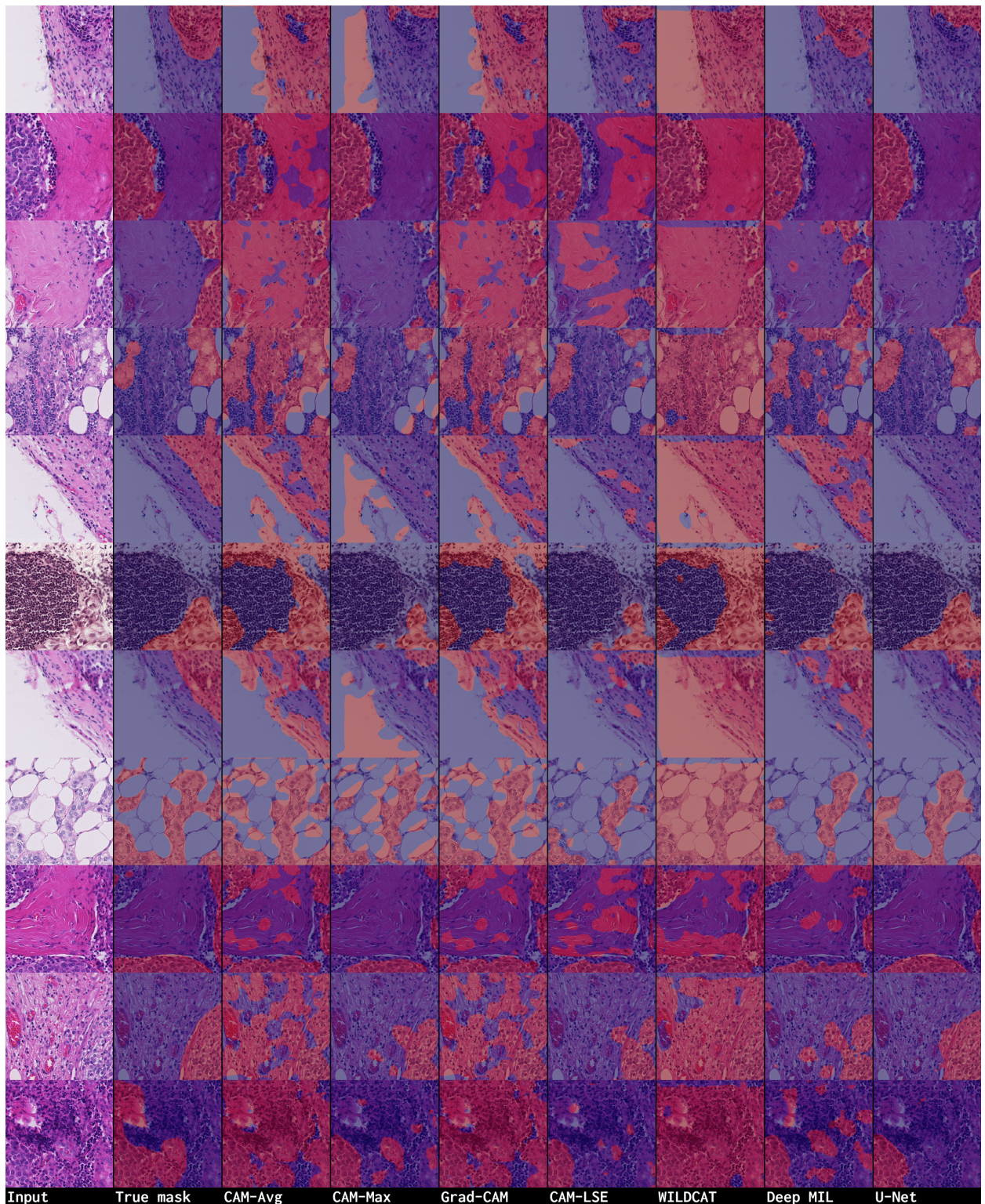


Figure A.21: Examples of visual comparison of the predicted binary mask of each WSOL method over CAMELYON16 test set (first split) for the metastatic class (patch size (1,024, 1,024)). (Best visualized in color.)